J. Fluid Mech. (1999), *vol.* 398, *pp.* 181–224. Printed in the United Kingdom

On the spatial evolution of a wall-imposed periodic disturbance in pipe Poiseuille flow at $Re = 3000$. Part 1. Subcritical disturbance

By B. MA[1], C. W. H. VAN DOORNE[2], Z. ZHANG[1] AND F. T. M. NIEUWSTADT[2]†

[1]Department of Engineering Mechanics, Tsinghua University, Beijing 100084, P. R. China
[2]J. M. Burgers Centre, Delft University of Technology, 2628 AL Delft, The Netherlands

(Received 3 August 1998 and in revised form 25 May 1999)

We have performed a numerical study on the transition of a cylindrical pipe flow under the influence of a localized disturbance in the form of periodic suction and blowing (PSB) applied at the pipe wall. We focus here on the so-called receptivity problem where the spatial evolution of this disturbance is studied as it travels downstream through the pipe. The study is carried out by means of two techniques: an eigenmode expansion solution (EES) and a full nonlinear direct numerical simulation (DNS). The EES is based on an analytical expansion in terms of the eigenfunctions of the linear operator which follows from the equations of motion expressed in a cylindrical coordinate system. The DNS is formulated in terms of a spectral element method.

We restrict ourselves to a so-called subcritical disturbance, i.e. the flow does not undergo transition. For very small amplitudes of the PSB disturbance the results of the EES and DNS techniques agree excellently. For larger amplitudes nonlinear interactions come into play which are neglected in the EES method. Nevertheless, the results of both methods are consistent with the following transition scenario. The PSB excites a flow perturbation that has the same angular wavenumber and frequency as the imposed disturbance itself. This perturbation is called the fundamental mode. By nonlinear self-interaction of this fundamental mode higher-order harmonics, both in the angular wavenumber and frequency, are generated. It is found that the harmonic with angular wavenumber 2, i.e. twice the wavenumber of the fundamental mode, and with zero frequency grows strongly by a linear process known as transient growth. As a result the (perturbed) pipe flow downstream of the disturbance region develops extended regions of low velocity, known as low-speed streaks. At large disturbance amplitudes these low-speed streaks show the development of high wavenumber oscillations and it is expected that at even higher disturbance amplitudes these oscillations become unstable and turbulent flow will set in.

Our result agrees (at least qualitatively) with the transition scenario in a plane Poiseuille flow as discussed by Reddy *et al.* (1998) and Elofson & Alfredson (1998).

1. Introduction

One of the most important discoveries made by Reynolds (1883) in his famous experiments is, expressed in his own words,

† Author to whom correspondence should be addressed: e-mail f.nieuwstadt@wbmt.tudelft.nl

> There were two critical values for the velocity in the tube,
> the one at which steady motion changed into eddies,
> the other at which eddies changed into steady motion.

To distinguish these critical values Reynolds introduced a dimensionless number $Re = \overline{U}D/\nu$ (with $\overline{U}$ the mean flow velocity, D the pipe diameter and ν the kinematic viscosity) which since then has carried his name. The first Reynolds number, at which steady motion changes into eddies, is called here the upper critical Reynolds number Re_{cru} whereas the second at which eddies change into steady motion is called the lower critical Reynolds number Re_{crl}. In between these two Reynolds numbers the flow can be either laminar or turbulent. In his original experiments, Reynolds found 12 830 for Re_{cru} and 2020 for Re_{crl}. Modern experiments have successfully raised Re_{cru} to 10^5 (see Draad, Kuiken & Nieuwstadt 1998 for a review). The Re_{crl}, however, has stayed close to its original value and is at present placed in the range $1760 < Re_{crl} < 2300$.

Theoretically, the upper bound of Re_{cru} can be obtained from linear stability theory but it is generally accepted that Hagen–Poiseuille flow is linearly stable with respect to all kinds of disturbances although a formal proof for non-axisymmetric infinitesimal disturbances is still not available (see Lessen, Sadler & Liu 1968; Salwen, Cotton & Grosch 1980 and Herron 1991 for the results of temporal stability theory; see Gill 1965 and Garg & Rouleau 1972 for the results of spatial stability theory). This sets the upper bound for Re_{cru} at infinity and it explains the large Re_{cru} observed in the experiments. A lower bound for Re_{crl} obtained from the energy method is found to be 81.49 (Joseph & Carmi 1969; Schmid & Henningson 1994) which differs strongly from the experimental values mentioned above. The big gap between theory and experiment reflects our currently poor understanding of the transition scenario of Hagen–Poiseuille flow. Even after more than a century since Reynolds' work and despite the efforts from numerous researchers this gap is still wide open. There are two important reasons for this:

1. The linear stability operator $\mathscr{L}$ of Hagen–Poiseuille flow is not self–adjoint. This is for instance the mathematical reason for the gap between Re_{cru} and Re_{crl} (see Dauchot & Manneville (1997)) and as a consequence a 'bifucation' transition scenario, known to be valid for Taylor–Couette or Rayleigh–Bénard flow, is not applicable here.

2. Linear stability theory provides no finite critical Reynolds number so that it becomes difficult to use a transition scenario based on 'secondary instability' which for instance has been successfully applied to plane Poiseuille flow and the Blasius boundary layer. (Davey & Nguyen 1971; Patera & Orszag 1981; Orszag & Patera 1983).

In order to make progress several theoretical alternatives have been considered which depart from a different base flow: the linear instability of the inlet flow (Tatsumi 1952) or the instability of a nearly circular elliptical pipe flow (Davey 1978 and Kerswell & Davey 1996). However, the experimental results of Wygnanski & Champagne (1973), Rubin, Wygnanski & Haritonidis (1980) and Darbyshire & Mullin (1995) suggest that the transition process is insensitive to the shape of the basic velocity profile on which the disturbances are introduced.

Another approach has been to rewrite the governing equations in terms of a non-self-adjoint linear operator $\mathscr{L}$ and to consider its potential to support large transient growth of the initial disturbance. This has been proposed recently as a possible scenario for shear flow transition (see Trefethen *et al.* 1993; Criminale *et al.* 1997 and the references therein). Although the original idea can be traced back to Kelvin (1887), its modern formulation in terms of a more elegant mathematical

language has led to fruitful results. Transient growth in cylindrical Poiseuille flow has been studied analytically by Bergström (1992, 1993*b*) and Schmid & Henningson (1994), experimentally by Bergström (1993*a*, 1995*b*) and numerically by Boberg & Brosa (1988) and by O'Sullivan & Breuer (1994*a*). Their conclusion is that significant transient growth of the initial kinetic energy can occur at an early stage of disturbance evolution, before the disturbance finally decays. A disturbance with unit azimuthal wavenumber and without streamwise dependence (in terms of temporal theory) has been found to have the largest amplification.

Despite transient growth, linear theory demands that a disturbance will finally decay. Therefore, a nonlinear instability mechanism is required to sustain the amplified disturbance towards turbulence. Such a process has been investigated in terms of various low-dimensional nonlinear models in order to explain the transition mechanism (see Waleffe 1997 and the references therein). For Hagen–Poiseuille flow, this has been done by Bergström (1995*a*, 1998) and Tumin (1997). In nearly all of these low-dimensional models the importance of an initial transient growth is emphasized. In a series of papers, Waleffe (1995*a*, *b*, 1997) proposes a self-sustaining process where three separate stages are identified. Transient growth plays a key role in the first stage to generate streamwise low-speed streaks. Zikanov (1996) has implemented this self-sustaining process in cylindrical Poiseuille flow and he finds that the modulated mean flow is highly unstable. This approach can actually be characterized as a 'secondary instability' theory where the secondary flow is provided by the linear transient effects instead of the Tollmien–Schlichting waves in the traditional 'secondary instability' theory.

In spite of the important role of transient growth in the models cited above, Dauchot & Manneville (1997) argue that this process is not a necessary component for transition. To support such a theoretical hypothesis evidence should be provided in terms of experimental and numerical results. Dauchot & Manneville (1997) themselves give different hints for 'natural' and 'triggered' transition experiments. The 'triggered' transition only corresponds to one special path in the phase space of their nonlinear model and each different initial parameter group corresponds to a different path.

Experiments on transitional pipe flow have mainly been concentrated on triggered transition since an experiment on so-called 'natural' transition would theoretically result in an infinite value for Re_{cru}. In all of these experiments, disturbances are introduced in the flow at the pipe wall. The equivalent experiment in the boundary layer is the 'vibrating ribbon' perturbation with well-known contributions by Schubauer & Skramstad (1947) and Klebanoff, Tidstrom & Sargent (1962). The flow development as a result of the introduced disturbance is generally denoted as the receptivity problem and this approach has been applied in studies of the boundary layer (Goldstein & Hultgren 1989). For pipe Poiseuille flow, the term 'receptivity' has been introduced by Tumin (1996). The early experiments on the transition in pipe flow did not consider the details of the imposed disturbance and their influence on the transition process. Since then it has been found that transition depends strongly on the disturbance details such as its amplitude, frequency and azimuthal wavenumber. Therefore, carefully calibrated experiments are necessary. Some first experiments giving data of sufficient detail have been performed recently by Darbyshire & Mullin (1995), Eliahou, Tumin & Wygnanski (1998) and Draad *et al.* (1998). In these experiments disturbances are introduced in the flow by means of periodic suction and blowing (PSB) at the pipe wall.

Another approach to obtain data on the transition process has been numerical simulation which is becoming more and more important as result of the increasing power of supercomputers (see Kleiser & Zang 1991 and Herbert 1991 for a review). Nevertheless only a few results are available. The reason is that a numerical simulation

of a PSB disturbance which is in principle a spatial evolution problem, requires enormous computer resources (Kleiser & Zang 1991). For plane Poiseuille flow, Danabasoglu, Biringen & Streett (1991) and Chung, Sung & Boiko (1997) have studied the spatial evolution of a PSB disturbance. They pay special attention to the active control of the inflow of Tollmien–Schlichting waves and not to the instability mechanism induced by the PSB disturbance itself. With respect to cylindrical pipe flow, Shan *et al.* (1999) have recently simulated the transition induced by PSB. They were able to reproduce successfully the structures experimentally observed in transitional pipe flow such as the 'puff' and 'slug' by introducing a local flow disturbance for a finite time. Further numerical data on the spatial evolution of disturbances in pipe flow are lacking. Such information is needed in order to explain the observed experimental phenomena and to supplement the shortage of experimental data.

In the present paper new numerical data are provided by performing a simulation study of the evolution of a PSB disturbance introduced at a localized region of the pipe wall. Our aim is not only to provide new numerical data on transitional pipe flow but more importantly to use the data obtained by two numerical techniques to study the modes that are involved in the reponse of the flow to the PSB disturbance. Based on these results, our objective is to propose a transition mechanism in cylindrical pipe flow.

The outline of this paper is as follows. In § 2 the governing equations for our problem are formulated. The eigenmode expansion is discussed in § 3. In § 4 the numerical scheme and code validation are presented. The results are presented in § 5 subdivided into a subsection in which we consider very small disturbance amplitudes for which a linear approximation is justified and a subsection for large disturbance amplitudes where nonlinear effects come into play. A discussion on the influence of various parameters is given in § 6. We end with some conclusions in § 7. Three Appendixes are added to provide further details about the formulation of the central boundary condition in a cylindrical coordinate system, the properties of the linear spatial evolution operator which describes the Hagen–Poiseuille flow and the derivation of the boundary-value problem in terms of eigenfunctions.

2. Formulation of the problem

2.1. *Governing equations*

The continuity equation and the Navier–Stokes equations for the flow of a Newtonian incompressible fluid expressed in vector notation read

$$\nabla \cdot \boldsymbol{v} = 0, \tag{2.1a}$$

$$\frac{\partial \boldsymbol{v}}{\partial t} + \boldsymbol{v} \cdot \nabla \boldsymbol{v} = -\nabla p + \frac{1}{Re}\nabla^2 \boldsymbol{v}, \tag{2.1b}$$

where $\boldsymbol{v}$ is the velocity vector and p the static pressure. For a cylindrical pipe with radius R, the laminar solution of (2.1) is the well-known parabolic Hagen–Poiseuille flow with $U_{\max}$ the maximum velocity on the centreline of the pipe. The equations (2.1) have been non-dimensionalized by R and $U_{\max}$, and the Reynolds number appearing in (2.1*b*) is the defined as $Re = U_{\max}R/\nu$ with ν the kinematic viscosity.

The Navier–Stokes equations written according to (2.1*b*) are expressed in the so-called 'convection form'. An alternative is the 'rotation form' given by

$$\frac{\partial \boldsymbol{v}}{\partial t} + \boldsymbol{\omega} \times \boldsymbol{v} = -\nabla \Pi + \frac{1}{Re}\nabla^2 \boldsymbol{v}, \tag{2.2}$$

where $\boldsymbol{\omega} = \nabla \times \boldsymbol{v}$ is the vorticity and $\Pi = p + \frac{1}{2}|\boldsymbol{v}|^2$ the total pressure. The 'rotation

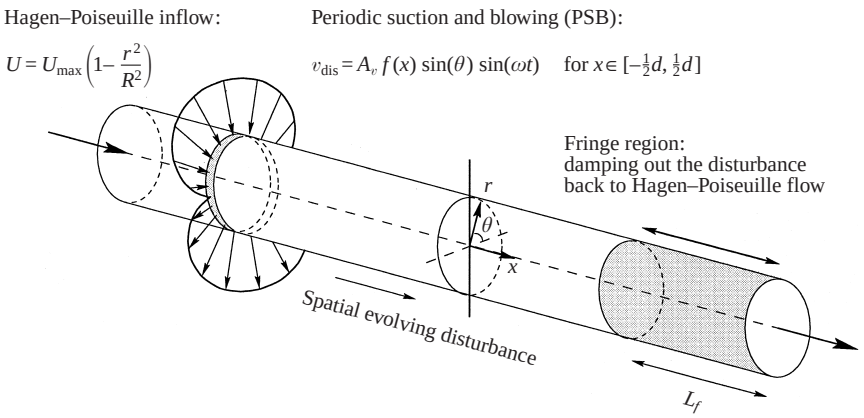

FIGURE 1. A sketch of the pipe geometry considered here; indicated are the inflow, the outflow, the PSB disturbance and the coordinate system used in the simulation.

form' is preferable for numerical simulation based on a spectral method such as we will use in this study because of its conservation properties and economical implementation (see Canuto *et al.* 1987, chapter 7).

We shall also use the component form of (2.1) formulated in terms of a cylindrical coordinate system where x, r and θ denote the axial, radial and azimuthal direction respectively and where $(\boldsymbol{e}_x, \boldsymbol{e}_r, \boldsymbol{e}_\theta)$ and (u, v, w) are the unit vectors and velocity components in these directions. The equations in this coordinate system read

$$\frac{\partial u}{\partial x} + \frac{1}{r}\frac{\partial (rv)}{\partial r} + \frac{1}{r}\frac{\partial w}{\partial \theta} = 0, \tag{2.3a}$$

$$\frac{\partial u}{\partial t} + u\frac{\partial u}{\partial x} + v\frac{\partial u}{\partial r} + \frac{w}{r}\frac{\partial u}{\partial \theta} = -\frac{\partial p}{\partial x} + \frac{1}{Re}\nabla^2 u, \tag{2.3b}$$

$$\frac{\partial v}{\partial t} + u\frac{\partial v}{\partial x} + v\frac{\partial v}{\partial r} + \frac{w}{r}\frac{\partial v}{\partial \theta} - \frac{w^2}{r} = -\frac{\partial p}{\partial r} + \frac{1}{Re}\left(\nabla^2 v - \frac{v}{r^2} - \frac{2}{r^2}\frac{\partial w}{\partial \theta}\right), \tag{2.3c}$$

$$\frac{\partial w}{\partial t} + u\frac{\partial w}{\partial x} + v\frac{\partial w}{\partial r} + \frac{w}{r}\frac{\partial w}{\partial \theta} + \frac{vw}{r} = -\frac{1}{r}\frac{\partial p}{\partial \theta} + \frac{1}{Re}\left(\nabla^2 w - \frac{w}{r^2} + \frac{2}{r^2}\frac{\partial v}{\partial \theta}\right), \tag{2.3d}$$

with

$$\nabla^2 = \frac{\partial^2}{\partial x^2} + \frac{1}{r}\frac{\partial}{\partial r}\left(r\frac{\partial}{\partial r}\right) + \frac{1}{r^2}\frac{\partial^2}{\partial \theta^2}.$$

The Hagen–Poiseuille profile mentioned above reads in this coordinate system

$$\boldsymbol{V}(r) = U(r)\boldsymbol{e}_x = (1 - r^2)\boldsymbol{e}_x, \qquad P(x) = P_0 - \frac{4}{Re}x. \tag{2.4a,b}$$

The capital letters $\boldsymbol{V}$, U and P are used to distinguish this profile as the basic flow on which we shall consider the development of disturbances in the next sections. P_0 is defined as the static pressure at $x = 0$.

2.2. *Boundary and initial conditions*

As mentioned in the introduction we consider the evolution of a disturbance imposed on the fundamental solution (2.4) in terms of periodic suction and blowing (PSB) through a slot located at some position along the pipe wall. A sketch of the geometry that we consider, is shown in figure 1.

For the PSB disturbance the wall boundary conditions become

$$r = 1: \quad u = w = 0, \quad v = v_{\text{dis}}(x, \theta, t) = A_v f(x) \sin(\theta) \sin(\omega t), \tag{2.5}$$

where ω is the disturbance frequency and A_v the disturbance amplitude. Note that this disturbance has angular wavenumber equal to one. A similar disturbance has been used in the experiments of Draad *et al.* (1998). The distribution of the velocity across the slot is given by a shape function $f(x)$ which is non-zero for $x \in [-\frac{1}{2}d, \frac{1}{2}d]$ with d the width of the PSB slot and with $x = 0$ as the centre of the PSB region. Draad *et al.* (1998) assumed that in their experiments $f(x)$ is constant and so did Tumin (1996). For numerical reasons we choose here

$$f(x) = \frac{1}{2}\left(\cos\frac{2\pi x}{d} + 1\right). \tag{2.6}$$

We will return to the shape function $f(x)$ in § 6 where we discuss the influence of various forms for $f(x)$. It follows directly from (2.5) that the instantaneous total disturbance mass flux is always equal to zero.

For the other boundary conditions we turn to the pipe centreline where the equations (2.3) are singular. This singularity must be removed to ensure a finite solution. To achieve this we impose a series of special constraints which the solution should satisfy when $r \to 0$ (see Appendix A).

As inflow condition we choose the Hagen–Poiseuille solution given by (2.4). This is an approximation since the upstream effects of the imposed disturbance may change the inflow from its parabolic form (see Appendix B, § B.3). Furthermore, in laboratory experiments an ideal Hagen–Poiseuille profile is not easily obtained (Draad & Nieuwstadt 1998). The outflow condition is implemented with help of the so-called fringe method (see § 4.1).

As initial condition, i.e. at the start of the PSB disturbance, we set everywhere the flow equal to the Hagen–Poiseuille profile (2.4*a*). Since we aim at the temporal asymptotic solution of (2.1), the initial condition should be not important. The laminar solution (2.4) seems a good choice since no additional initial disturbance will be introduced so that possible temporal transients which can contaminate our spatial analysis are avoided.

3. Eigenmode expansion

In view of the form of the disturbance velocity (2.5) we expect that the flow modes generated by this disturbance can be expressed in terms of Fourier functions with an azimuthal wavenumber m and a circular frequency $n\omega$. Let us denote these flow modes by the number pair (m, n). The mode $(\pm 1, \pm 1)$ which has the same angular and time dependence as the disturbance is called the fundamental mode. The temporal asymptotic response of (2.1) to the disturbance can then be written as the sum of the fundamental disturbance modes and their harmonics (see Gaster 1965 for discussion of this assumption for the case of a boundary layer). In the following we shall denote this approach as the eigenmode expansion solution (EES). The formal solution of (2.1) and (2.5) can now be expressed by the following double Fourier series:

$$\boldsymbol{v}(r, \theta, x, t) = \boldsymbol{V}(r) + \sum_{m=-\infty}^{\infty} \sum_{n=-\infty}^{\infty} \hat{\boldsymbol{v}}(r, x; m, n) \mathrm{e}^{\mathrm{i}(m\theta - n\omega t)}, \tag{3.1a}$$

$$p(r,\theta,x,t) = P(x) + \sum_{m=-\infty}^{\infty}\sum_{n=-\infty}^{\infty} \hat{p}(r,x;m,n)\mathrm{e}^{\mathrm{i}(m\theta - n\omega t)}, \tag{3.1b}$$

where $\boldsymbol{V}(r)$ and $P(x)$ denote the basic solution (2.4). Note that (3.1) is not applicable to a turbulent solution since in that case the temporal behaviour is not governed by a periodicity with frequency ω as in (3.1). Thus, (3.1) is only valid for the situation when no transition to turbulence occurs.

Given the fact that both the velocity $\boldsymbol{v}$ and the pressure p are real variables it can be shown from (3.1) that

$$\hat{\boldsymbol{v}}(r,x;-m,-n) = \hat{\boldsymbol{v}}^*(r,x;m,n), \quad \hat{p}(r,x;-m,-n) = \hat{p}^*(r,x;m,n), \tag{3.2}$$

where the superscript $*$ denotes the complex conjugate.

By substitution of (3.1) in (2.3) the equations (2.3) can be transformed from physical space (θ,t) to Fourier spectral space (m,n). The result reads

$$\frac{\partial \hat{u}}{\partial x} + \frac{1}{r}\frac{\partial (r\hat{v})}{\partial r} + \frac{\mathrm{i}m}{r}\hat{w} = 0, \tag{3.3a}$$

$$-\mathrm{i}n\omega\hat{u} + U\frac{\partial \hat{u}}{\partial x} + \hat{v}\frac{\mathrm{d}U}{\mathrm{d}r} + N_x = -\frac{\partial \hat{p}}{\partial x} + \frac{1}{Re}\hat{\nabla}^2\hat{u}, \tag{3.3b}$$

$$-\mathrm{i}n\omega\hat{v} + U\frac{\partial \hat{v}}{\partial x} + N_r = -\frac{\partial \hat{p}}{\partial r} + \frac{1}{Re}\left(\hat{\nabla}^2\hat{v} - \frac{1}{r^2}\hat{v} - \frac{2\mathrm{i}m}{r^2}\hat{w}\right), \tag{3.3c}$$

$$-\mathrm{i}n\omega\hat{w} + U\frac{\partial \hat{w}}{\partial x} + N_\theta = -\frac{\mathrm{i}m}{r}\hat{p} + \frac{1}{Re}\left(\hat{\nabla}^2\hat{w} - \frac{1}{r^2}\hat{w} + \frac{2\mathrm{i}m}{r^2}\hat{v}\right), \tag{3.3d}$$

where

$$\hat{\nabla}^2 = \frac{\partial^2}{\partial x^2} + \frac{1}{r}\frac{\partial}{\partial r}\left(r\frac{\partial}{\partial r}\right) - \frac{m^2}{r^2}.$$

The N_x, N_r, N_θ are components of the transformed nonlinear term which in spectral space takes the form of a convolution product according to

$$\boldsymbol{N}(r,x;m,n) = \sum_{i+j=m}\sum_{k+l=n} \hat{\boldsymbol{v}}(r,x;i,k)\cdot\boldsymbol{\mathcal{G}}(r,x;j,l),$$

with the velocity gradient tensor $\boldsymbol{\mathcal{G}}$ given by

$$\boldsymbol{\mathcal{G}} = \hat{\nabla}\hat{u}\,\boldsymbol{e}_x + \hat{\nabla}\hat{v}\,\boldsymbol{e}_r + \hat{\nabla}\hat{w}\,\boldsymbol{e}_\theta + \frac{1}{r}(-\hat{w}\,\boldsymbol{e}_\theta\boldsymbol{e}_r + \hat{v}\,\boldsymbol{e}_\theta\boldsymbol{e}_\theta),$$

where

$$\hat{\nabla} = \frac{\partial}{\partial x}\boldsymbol{e}_x + \frac{\partial}{\partial r}\boldsymbol{e}_r + \frac{\mathrm{i}j}{r}\boldsymbol{e}_\theta.$$

By introducing two auxiliary variables, namely $\hat{v}_x = \partial\hat{v}/\partial x$, $\hat{w}_x = \partial\hat{w}/\partial x$, and by substituting (3.3*a*) into (3.3*b*), the equation system (3.3) can be rewritten as a first-order differential equation in x which describes a spatial evolution problem. The resulting system can then be expressed as

$$\frac{\partial \boldsymbol{F}}{\partial x} = \mathscr{L}\boldsymbol{F} + \boldsymbol{S}, \tag{3.4}$$

where $\mathscr{L}$ is the spatial linear evolution operator, $\boldsymbol{F} = (\hat{u},\hat{v},\hat{w},-Re\,\hat{p},\hat{v}_x,\hat{w}_x)^{\mathrm{T}}$ the solution vector and $\boldsymbol{S} = Re\,(0,0,0,N_x,N_r,N_\theta)^{\mathrm{T}}$ the nonlinear interaction term (for further details about the operator $\mathscr{L}$ refer to Appendix B or Tumin 1996). In the Appendix B we also consider the eigenvalue problem for the linear operator $\mathscr{L}$. Its

eigenvalues and eigenfunctions denoted as $(\alpha, \boldsymbol{F}_\alpha)$, are used below to formulate an analytical solution of (3.4)

The wall boundary conditions (2.5) in spectral space become

$$r = 1: \quad \boldsymbol{F}_1 = \boldsymbol{F}_3 = 0, \ \boldsymbol{F}_2 = \phi_{mn} A_v f(x), \tag{3.5}$$

where

$$\phi_{mn} = \begin{cases} \frac{1}{4}mn & \text{when } (m,n) = (\pm 1, \pm 1) \\ 0 & \text{when } (m,n) \neq (\pm 1, \pm 1). \end{cases}$$

For the conditions at the pipe centre where the solution $\boldsymbol{F}$ should remain finite, refer again to Appendix A.

The system (3.4) and its associated boundary condition (3.5) is known as a receptivity problem (Tumin 1996). Let us consider a solution of this problem in terms of an expansion in the eigenmodes of $\mathscr{L}$ mentioned above. The system (3.4) for different Fourier modes (m, n) is coupled by the nonlinear interaction term $\boldsymbol{S}$ which in principle leads to an analytically intractable problem. However, if we limit ourselves to a disturbance with small amplitude $A_v \ll 1$, the source term $\boldsymbol{S}$ can be simplified or even neglected by dropping some or all of the high-order nonlinear terms, the details of which will be discussed in § 3.1 and § 3.2. With $A_v \ll 1$ the formal solution of (3.4) and (3.5) can be obtained by applying a standard eigenmode expansion technique which leads to the expression

$$\boldsymbol{F}(r, x; m, n) = \sum_\alpha X_\alpha(x) \boldsymbol{F}_\alpha(r; m, n), \tag{3.6}$$

where $X_\alpha(x)$ is a coefficient function and the summation runs over all eigenvalues α (with $\alpha = \alpha_\mathrm{r} + \mathrm{i}\alpha_\mathrm{i}$) of the operator $\mathscr{L}$ for mode (m, n). This form will be denoted in the following as the eigenmode expansion solution (EES). If all eigenmodes are stable, the above expansion is valid everywhere for $x \in (-\infty, \infty)$; otherwise it is valid in any finite x-interval.

The eigenvalues and their corresponding eigenfunctions $\boldsymbol{F}_\alpha$ for the modes $(m, n) = (\pm 1, \pm 1), (\pm 2, 0)$ and $(0, 0)$ and for $\omega = 0.4$ and $Re = 3000$ are discussed in detail in Appendix B where we also introduce the adjoint eigenvector $\boldsymbol{G}_\alpha$ which is different from $\boldsymbol{F}_\alpha$ due to the non-normality of the operator $\mathscr{L}$. However, some further remarks regarding the properties of the eigenvalues α and their eigenmodes may be appropriate here. Together with the frequency ω introduced in the Fourier expansion (3.1), the real part α_r of the eigenvalue α gives the phase velocity of the waves in which the disturbance is expanded. The imaginary part α_i denotes the amplification factor. For $\omega > 0$ a positive value of α_r implies a downstream travelling wave or a positive phase speed. If the propagation of the eigenmode, which is determined by the group velocity, is now in the same direction as the phase velocity, $\alpha_\mathrm{i} > 0$ would mean a stable mode and $\alpha_\mathrm{i} < 0$ an unstable mode. Although it has not been formally proven, it is nevertheless accepted that all linear modes in cylindrical pipe flow are stable and this is confirmed by our own DNS results. This means that for all downstream moving modes $\alpha_\mathrm{i} > 0$ and for all upstream moving modes $\alpha_\mathrm{i} < 0$. Most of the earlier work on spatial stability theory has been restricted to the downstream propagating modes. However, in Appendix B, § B.3 where further details are presented, we show that the upstream propagating modes cannot be neglected in this case and that they should be taken into account for a complete description of the disturbance evolution.

Given the formulation of the solution of (3.4) in terms of eigenmodes we now consider the approximation of the nonlinear interaction term $\boldsymbol{S}$ based on the constraint

that $A_v \ll 1$. We distinguish between the fundamental modes $(m,n) = (\pm 1, \pm 1)$ and the other modes $(m,n) \neq (\pm 1, \pm 1)$.

3.1. *Fundamental modes* $(m,n) = (\pm 1, \pm 1)$

Given that $A_v \ll 1$ we can simply drop the nonlinear term $\boldsymbol{S}$ in the equation for the fundamental modes by assuming that the amplitudes of the other Fourier modes $(m,n) \neq (\pm 1, \pm 1)$ are at most of the same order of magnitude as the $(\pm 1, \pm 1)$ modes so that their contribution through the quadratic nonlinear term is negligible. The fundamental modes $(\pm 1, \pm 1)$ thus satisfy linear equation

$$\frac{\partial \boldsymbol{F}}{\partial x} = \mathscr{L}\boldsymbol{F}. \tag{3.7}$$

As result of a standard eigenmode expansion applied to (3.7), we obtain an ordinary differential equation (ODE) for $X_\alpha(x)$ given by

$$\frac{\mathrm{d}X_\alpha}{\mathrm{d}x} = \mathrm{i}\alpha X_\alpha + A_v C_\alpha f, \tag{3.8}$$

where $C_\alpha = -\phi_{mn} G^*_{\alpha 1}|_{r=1}$ with $G_{\alpha 1}$ the first component of the adjoint eigenvector $\boldsymbol{G}_\alpha$. For a derivation of (3.8) refer to Appendix C.

The solution of (3.8) can be expressed as

$$X_\alpha(x) = A_v C_\alpha f_\alpha(x)\, \mathrm{e}^{\mathrm{i}\alpha x},$$

where

$$f_\alpha(x) = \int_{x_0}^{x} f(z)\, \mathrm{e}^{-\mathrm{i}\alpha z}\, \mathrm{d}z. \tag{3.9}$$

For downstream propagating modes with $\alpha_\mathrm{i} \geqslant 0$ the initial point x_0 becomes equal to $-\infty$ which means that at x only influence from the interval $(-\infty, x]$ can be felt. Similarly, for the upstream propagating modes with $\alpha_\mathrm{i} \leqslant 0$, the initial point $x_0 = \infty$. Note that we also use the assumption that all the eigenmodes will decay so that $X_\alpha(-\infty) = X_\alpha(\infty) = 0$.

The solution of (3.7) and (3.5) can then be expressed as

$$\boldsymbol{F}(r,x;m,n) = A_v \sum_\alpha C_\alpha f_\alpha(x) \boldsymbol{F}_\alpha(r;m,n)\, \mathrm{e}^{\mathrm{i}\alpha x}. \tag{3.10}$$

Given the discussion above, we find that the solution of the fundamental modes is linearly dependent on the forcing amplitude A_v. Therefore, when we consider the kinetic energy of the disturbance energy (see § 5.1), it should be scaled with A_v^2.

3.2. *Harmonic modes* $(m,n) \neq (\pm 1, \pm 1)$

To generate modes other than the fundamental we must take into account the nonlinear interaction term $\boldsymbol{S}$ or alternatively the convolution product $\boldsymbol{N}$. Given that $A_v \ll 1$, $\boldsymbol{N}$ can be decomposed as $\boldsymbol{N} = \boldsymbol{N}_O + \boldsymbol{N}_o$ where $\boldsymbol{N}_O$ stands for a self-interaction of only the fundamental modes $(m,n) = (\pm 1, \pm 1)$ and $\boldsymbol{N}_o$ for all other interactions. It then follows that $\boldsymbol{N}_O(r,x;m,n) = O(\hat{\boldsymbol{v}}(r,x;\pm 1,\pm 1)^2)$ and $\boldsymbol{N}_o(r,x;m,n) = o(\hat{\boldsymbol{v}}(r,x;\pm 1,\pm 1)^2)$. Consequently, $\boldsymbol{N}_o$ can be considered as a high-order term with respect to $\boldsymbol{N}_O(r,x;m,n)$ and can thus be neglected. The equation system (3.4) for mode (m,n) can be then simplified to

$$\frac{\partial \boldsymbol{F}}{\partial x} = \mathscr{L}\boldsymbol{F} + \boldsymbol{S}_O, \tag{3.11}$$

where $\boldsymbol{S}_O = Re\,(0,0,0,N_{Ox},N_{Or},N_{O\theta})^{\mathrm{T}}$ is the source term which describes the contribution to mode (m,n) by the quadratic nonlinear self-interaction of the fundamental modes $(m,n) = (\pm1,\pm1)$. The convolution product $\boldsymbol{N}_O$ can be evaluated from the solution for modes $(\pm1,\pm1)$ according to

$$\begin{aligned}
\boldsymbol{N}_O(r,x;\,0,\,0) &= \sum_{i=\pm1}\sum_{k=\pm1} \hat{\boldsymbol{v}}(r,x;i,k)\cdot\mathscr{G}(r,x;-i,-k),\\
\boldsymbol{N}_O(r,x;\,0,\pm2) &= \sum_{i=\pm1} \hat{\boldsymbol{v}}(r,x;i,\pm1)\cdot\mathscr{G}(r,x;-i,\pm1),\\
\boldsymbol{N}_O(r,x;\pm2,\,0) &= \sum_{k=\pm1} \hat{\boldsymbol{v}}(r,x;\pm1,k)\cdot\mathscr{G}(r,x;\pm1,-k),\\
\boldsymbol{N}_O(r,x;\pm2,\pm2) &= \hat{\boldsymbol{v}}(r,x;\pm1,\pm1)\cdot\mathscr{G}(r,x;\pm1,\pm1).
\end{aligned}$$

This results implies that by self-interaction of the fundamental modes four additional modes are generated, namely $(0,0)$, $(0,\pm2)$, $(\pm2,0)$ and $(\pm2,\pm2)$. In the following we will call mode $(0,0)$ the mean perturbation mode and $(\pm2,0)$ the steady harmonic. For convenience, we will denote hereafter the nine harmonic modes generated by self-interaction as (m_2,n_2) and for the notation of the four fundamental modes we use (m_1,n_1). Since modes (m_1,n_1) are decoupled from all others modes, it follows that the harmonic modes are also decoupled and can thus be calculated individually.

A similar approach as used to derive the equations for (m_2,n_2), can be applied to obtain equations for the higher-order modes beyond (m_2,n_2) but the procedure becomes quite complicated. We stop here since those higher-order modes are assumed to be not as important as (m_1,n_1) and (m_2,n_2).

For the modes (m_2,n_2) the boundary conditions (3.5) are homogeneous so that a non-trivial solution depends on the source term $\boldsymbol{S}_O(r,x)$. In order to find this solution, the source term $\boldsymbol{S}_O(r,x)$ must first be expanded as a summation of the eigenvectors $\boldsymbol{F}_\alpha(r;m,n)$ according to

$$\boldsymbol{S}_O(r,x) = \sum_\alpha h_\alpha(x)\boldsymbol{F}_\alpha(r;m,n),$$

where

$$h_\alpha(x) = \int_0^1 r\boldsymbol{G}_\alpha^\dagger(r)\boldsymbol{S}_O(r,x)\,\mathrm{d}r,$$

and where the superscript † denotes the Hermitian adjoint of the adjoint eigenvector $\boldsymbol{G}_\alpha$.

Following a similar approach as for modes $(\pm1,\pm1)$, the solution of (3.11) can then be obtained as

$$\boldsymbol{F}(r,x) = \sum_\alpha g_\alpha(x)\boldsymbol{F}_\alpha(r)\mathrm{e}^{\mathrm{i}\alpha x}, \tag{3.12}$$

where

$$g_\alpha(x) = \int_{x_0}^{x} h_\alpha(z)\mathrm{e}^{-\mathrm{i}\alpha z}\,\mathrm{d}z,$$

with again $x_0 = -\infty$ when $\alpha_\mathrm{i} \geqslant 0$ and $x_0 = \infty$ when $\alpha_\mathrm{i} \leqslant 0$.

Since the harmonic modes (m_2,n_2) are generated by the quadratic nonlinear interaction of the fundamental modes which themselves scale with A_v, the kinetic energy of these harmonics should then be scaled with A_v^4.

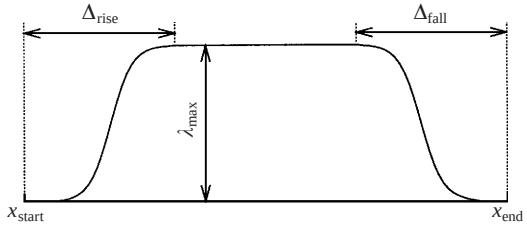

FIGURE 2. Fringe function $\lambda(x)$ in the fringe region. The fringe region extends from x_{start} to x_{end} and $\lambda_{\max}$ is the maximum value of $\lambda(x)$. Δ_{rise}, Δ_{fall} are regions where $\lambda(x)$ rises from zero to its maximum value or drops back from its maximum value to zero.

4. Numerical techniques and solution procedure

4.1. *Direct numerical simulation*

In this subsection we consider the numerical solution of the full set of nonlinear equations (2.1*a*) and (2.2). The point of departure is a spectral code that has been used to simulate a puff and slug in transitional pipe flow and for more information we refer to Shan *et al.* (1999). Keeping the main structure of the code unchanged, we have rewritten it in order to run on a parallel computer. Furthermore, a fringe method has been implemented to accommodate a spatially evolving disturbance. Below we will give some further details.

The spatial discretization is based on a spectral method applied to the governing equations in cylindrical coordinates formulated in their 'rotation' form. Given the natural periodicity in the azimuthal direction we adopt in this direction a Fourier collocation method. The singular behaviour at $r = 0$ related to the cylindrical coordinate system results in a very fine grid in the azimuthal direction when $r \to 0$. In view of numerical stability conditions this fact puts a strong restriction on our time step. To circumvent this problem a spectral element approach is applied in the radial direction with a single cylindrical element at the centre and annular elements surrounding it. The outer boundaries of these elements are given by

$$r_j = (1 - r_c)\left\{\ln\left[\frac{N_e - j}{N_e - 1}(\mathrm{e} - 1) + 1\right]\right\}^{1/2} + r_c, \tag{4.1}$$

where $j = 1, 2, \ldots N_e$ are the indices of the elements and r_c the radius of the central cylindrical element. Inside each element, a Chebyshev collocation method is used with Gauss–Lobatto collocation points. In the axial direction we also apply a Fourier collocation method which means that our solution should be periodic in the axial direction. Periodicity in the axial direction is at variance with the streamwise spatial evolution of an imposed disturbance. To restore the periodicity we apply a so-called fringe region at the end of the computational domain.

The fringe method used here has been proposed by Lundbladh *et al.* (1994). The main task of a fringe region is to force the velocity profile near the outflow to a prescribed inflow profile with minimal reflection. This is achieved by dividing the computational domain into two regions in the streamwise direction: a region where the Navier–Stokes equations (2.2) are left unmodified and which we will use to study the development of the flow disturbance; and a fringe region where the equations are modified by including a forcing term in the equations of motion. For this forcing term we take $\lambda(x)(\boldsymbol{u} - \boldsymbol{v})$ which is added to the right-hand-side of (2.2). The $\boldsymbol{u}$ is a prescribed

velocity and $\lambda(x)$ the so-called fringe function. For more information about the fringe method see Lundbladh *et al.* (1994) and Nordström, Nordin & Henningson (1997).

The fringe function $\lambda(x)$ is chosen such that the velocity $\boldsymbol{v}$ approaches gradually the prescribed velocity $\boldsymbol{u}$ at the end of the fringe region. In figure 2, the fringe function $\lambda(x)$ we have used in our simulations is shown. In particular we have chosen $\Delta_{\text{rise}} = \frac{5}{16}L_f$ and $\Delta_{\text{fall}} = \frac{3}{16}L_f$ where $L_f = x_{\text{end}} - x_{\text{start}}$ is the total length of the fringe region. The prescribed velocity $\boldsymbol{u}$ which can in principle be chosen freely within the constraint of a divergence-free flow field, is for our case the parabolic profile (2.4). Periodicity is now satisfied and the Fourier spectral method can be applied.

Based on the results of Lundbladh *et al.* (1994), we can estimate the factor by which this disturbance velocity is damped after entering the fringe region. This factor is

$$f_d = \exp\left[\frac{1}{c}\int_{x_{\text{start}}}^{x_{\text{end}}} \lambda(x)\,\mathrm{d}x\right] = \exp\left[\frac{\lambda_{\max}}{c}\left(L_f - \frac{\Delta_{\text{rise}} + \Delta_{\text{fall}}}{2}\right)\right] = \exp\left(\frac{3}{4}\frac{\lambda_{\max}L_f}{c}\right),$$

where c is the propagation speed of the disturbance which is taken equal to $U_{\max}$ in our case. In our simulation f_d is always chosen to be more than 10^6.

It is desirable to keep the fringe length L_f as short as possible but when the damping rate f_d remains fixed, a shorter L_f corresponds to a larger $\lambda_{\max}$. The value of $\lambda_{\max}$ is restricted, however, because in our simulation the forcing of the fringe is imposed in the advection time step which is discretized in terms of an explicit algorithm. Therefore, the magnitude of $\lambda_{\max}$ is limited due to stability considerations which means that L_f has a lower bound.

The spatially discretized system of equations is integrated as a function of time by means of a time-splitting method with the help of a stiffly stable scheme (Karniadakis, Israeli & Orszag 1991). The so-called 'time-splitting errors' which violate the divergence-free constraint near the boundary are removed by using an improved pressure boundary condition (Tomboulides, Israeli & Karniadakis 1989; Karniadakis *et al.* 1991) and by applying the Green's function correction (Marcus 1984). The non-linear term $\boldsymbol{v}\times\boldsymbol{\omega}$ is evaluated by means of a pseudo-spectral technique and de-aliased with the help of the $\frac{3}{2}$-rule.

The PSB region where the disturbance is added to the flow is centred at $x_c^* = 1.5\pi$ with $d = \pi$ as its width. The notation x^* denotes the coordinate used in our numerical computations which has its origin at the inflow cross-section of the calculation domain (note that the coordinate x which we will use to present our results has its origin at the centre of the disturbance region, x_c^*). For a discussion of the location of the PSB region and its effects we refer to Appendix B, § B.3.

4.2. *Computational details*

We have carried out several computations with the DNS code using various values for A_v. The details are given in table 1 where we also indicate the number of grid points that we have used in each coordinate direction. In order to compare our resolution with previous numerical simulations we present the grid size normalized in terms of so-called viscous wall units as indicated by a superscript $+$. The pipe radius in this normalization becomes $R^+ \approx 114.5$. In the radial direction the first grid point from wall lies at $y^+ \approx 0.125$. The maximum grid spacing in the radial direction is located at the pipe centre and is equal to $\Delta y^+ \approx 6.767$. This radial resolution is comparable with the well-resolved simulation of a turbulent channel flow given by Kim, Moin & Moser (1987). For the azimuthal direction with the highest resolution ($n_\theta = 32$), the grid spacing reaches a minimum value $(\Delta r\Delta\theta)^+ \approx 0.33$ near centreline and maximum

A_v	$n_x \times n_r \times n_\theta$	L_x	L_f
0.001	$128 \times 53 \times 16$	32π	4π
0.015	$128 \times 53 \times 16$	32π	8π
0.025	$128 \times 53 \times 16$	32π	8π
0.03	$128 \times 53 \times 16$	32π	4π
0.031	$128 \times 53 \times 32$	32π	8π
0.0325	$512 \times 53 \times 32$	32π	8π

TABLE 1. Computational details for DNS realizations used in this paper. A_v is the disturbance amplitude, n_x, n_r and n_θ are the numbers of grid points in the axial, radial and azimuthal directions respectively (including the grid points in fringe region), L_x is the length of pipe and L_f the length of fringe region. The minimum grid spacing in the r-direction $\Delta r_{\min} = 0.0011$ while the maximum value $\Delta r_{\max} = 0.0591$. In all simulations, four spectral elements are used in the radial direction with the radius of the central element $r_c = 0.1$. With five collocation points for the central element and seventeen collocation points for the other elements, the number of radial grid points becomes $n_r = (4-1) \times (17-1) + 5 = 53$.

value $(R\Delta\theta)^+ \approx 22.49$ at wall. This azimuthal resolution is somewhat worse than the well-resolved turbulent pipe flow simulation given by Eggels *et al.* (1994).

The bottleneck is the spatial resolution in the axial direction where we have the longest spatial extent. Zang, Krist & Hussaini (1989) have shown that the effect of resolution can be very large. This is confirmed by our own experience and an example of the effect of resolution is shown in figure 3. We see that for a coarse resolution transition occurs and the flow becomes turbulent whereas for the largest resolution the flow stays laminar. In the following sections we shall only present results obtained for each A_v at the highest resolution as given in table 1 for which we are confident to have obtained a grid-independent solution.

The DNS has been carried out on the 10 processor Cray-J90 of the Delft University of Technology and on the 12 processor Cray-C90 of the Academic Computing Services Center (SARA) in Amsterdam.

4.3. *Code verification*

The original code for temporal simulation has been extensively tested for its algorithm performance and stability properties (Shan *et al.* 1999). Here, we have carried out some additional verification for the new code which concerns the efficiency of parallellization and its ability to simulate the spatial evolution of a disturbance.

Parallel efficiency

In figure 4 the speed-up of the parallel DNS code is shown based on the run-time record of a computation on a Cray J90. The overhead when using more CPUs is partially due to the imperfect running environment where we have to share CPUs with other users. Given this fact, the efficiency of the parallellization is quite satisfying. In most of our calculations we have used four CPUs.

Evolution of the least stable mode

A simple method to test the DNS code for its ability to simulate the evolution of a disturbance is to perform a computation of the evolution of the least stable eigenmode obtained from spatial linear stability theory (for a general review on linear stability refer to Drazin & Reid 1981 and also to Appendix B for some special results concerning the Hagen–Poiseuille flow that we consider here). To generate the

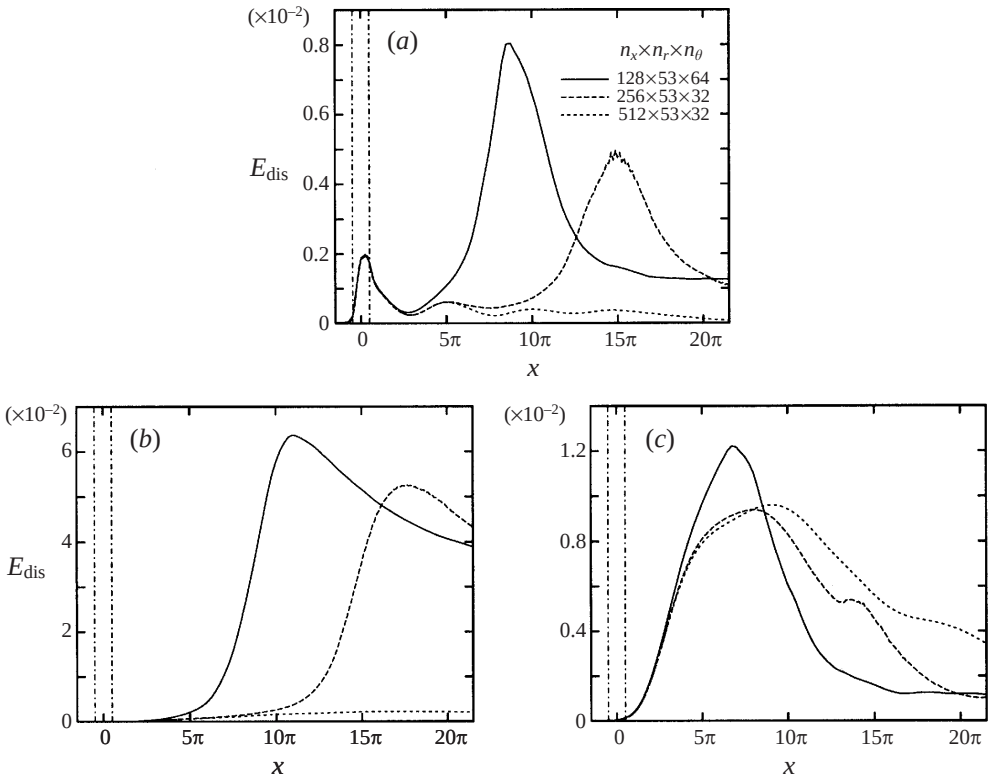

FIGURE 3. Disturbance energy $E_{dis}(x)$ for the case $A_v = 0.0325$ as a function of x for different modes and different numerical spatial resolution as indicated: (*a*) $(m, n) = (\pm 1, \pm 1)$; (*b*) $(m, n) = (\pm 2, 0)$ and (*c*) $(m, n) = (0, 0)$. The – – – indicates PSB region. See § 5.1 for the introduction of disturbance energy E_{dis}.

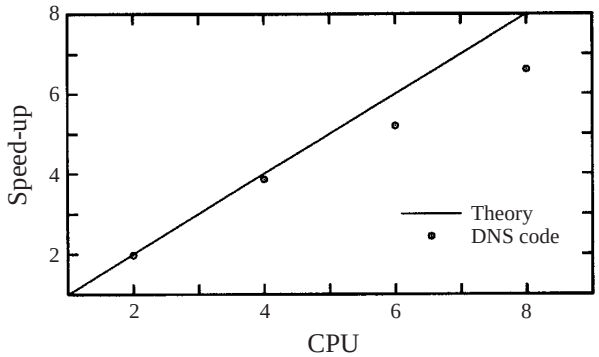

FIGURE 4. Speed-up for $128 \times 53 \times 16$ mesh on a Cray J90. The speed-up is defined as the CPU time per time step on one processor divided by the CPU time per time step on more than one processor.

forcing term in our fringe method, we take a linear combination of the least stable eigenmodes at $Re = 3000$ with $(m, \omega) = (\pm 1, \pm 0.5)$. The combination is chosen such that a real velocity field $\boldsymbol{u}$ is generated as required by our DNS code. The amplitude of this flow field should be chosen sufficiently small so that nonlinear effects may be neglected.

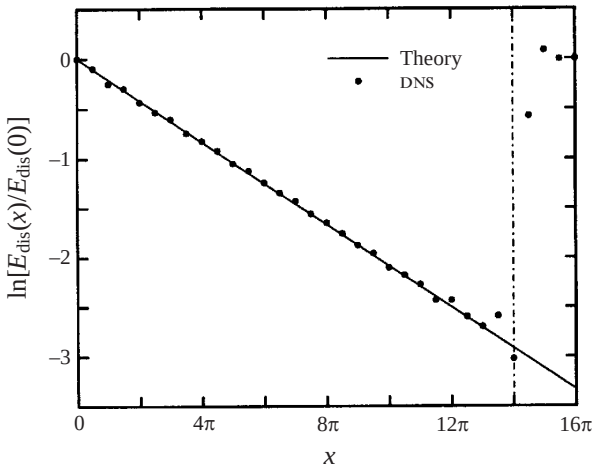

FIGURE 5. Spatial evolution of the disturbance energy $E_{dis}(x)$ for the least stable eigenmode ($m = 1, \omega = 0.5, Re = 3000$. DNS mesh is $32 \times 53 \times 16$; the dash-dotted vertical line indicates the start of the fringe region).

The evolution of the eigenmodes is governed by the imaginary part α_i of the eigenvalue α which leads to an exponential decay of the disturbance energy (see § 5.1) with exponent $-2\alpha_i$. The results obtained with the DNS are shown in figure 5 in comparison with this exponential decay. From the computed results we estimate α_i as $\frac{1}{2}\ln[E_{dis}(x)/E_{dis}(0)]/x$ with as result $\alpha_i = -0.03293 \pm 0.00056$ while from linear theory one finds $\alpha_i = -0.03315$. The agreement is quite acceptable and is taken as proof of the correctness of our code.

This test case also shows the capability of the fringe method to restore the flow to the given inflow condition. This can be seen in figure 5 where in the fringe region the disturbance energy returns to the energy of the inflow profile. Furthermore, the calculation shows that the influence of reflection by the fringe region is limited to a region with a length of about $\frac{1}{2}L_f$ in front of the fringe region.

Comparison between the EES and DNS solution

In this subsection we consider the solution of both the DNS and the EES for a disturbance velocity according to (2.5) with $A_v \ll 1$. This can be considered as a verification of both methods.

In § 5.2 the results of the DNS and the EES will be considered in full detail in particular with respect to the evolution of disturbances downstream of the disturbance region. Therefore, we will limit ourselves here to the results at three important x-positions within the disturbance region itself, namely $x = \pm\frac{1}{2}\pi$ and $x = 0$ which are the two edges and the centre point. For the DNS we take $A_v = 10^{-3}$. Note that the solution of the EES is in principle independent of A_v. The two edges of the PSB region, i.e. $x = \pm\frac{1}{2}\pi$, are actually the lower or upper limit of the integral (3.9) since $f(x)$ is zero outside the PSB region. This means for $x = -\frac{1}{2}\pi$, i.e. the left edge of the PSB region, that there can be no downstream travelling eigenmodes and for $x = \frac{1}{2}\pi$, i.e. the right edge, no upstream travelling eigenmodes. At the centre of the PSB region, $x = 0$, a large number of eigenmodes are excited each with comparable amplitudes. Therefore it will turn out to be difficult to obtain an accurate solution at this position with the linear eigenmode expansion method.

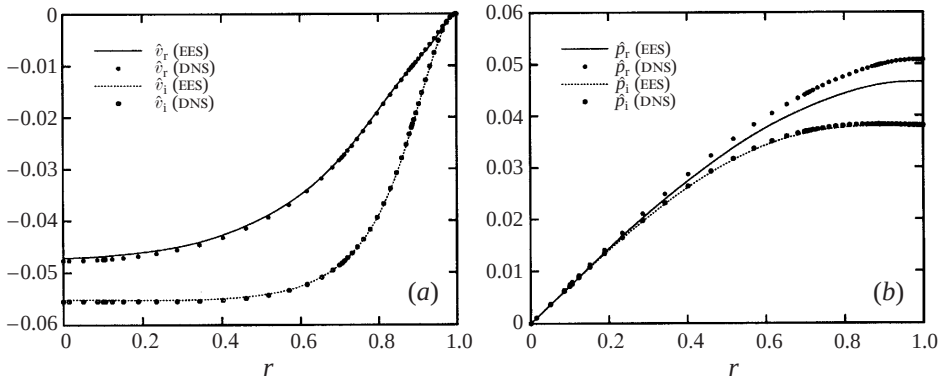

FIGURE 6. The profiles of radial velocity $\hat{v}$ and pressure $\hat{p}$ of mode $(1,1)$ at $x = \frac{1}{2}\pi$, the right-hand edge of the PSB region ($Re = 3000, \omega = 0.5$).

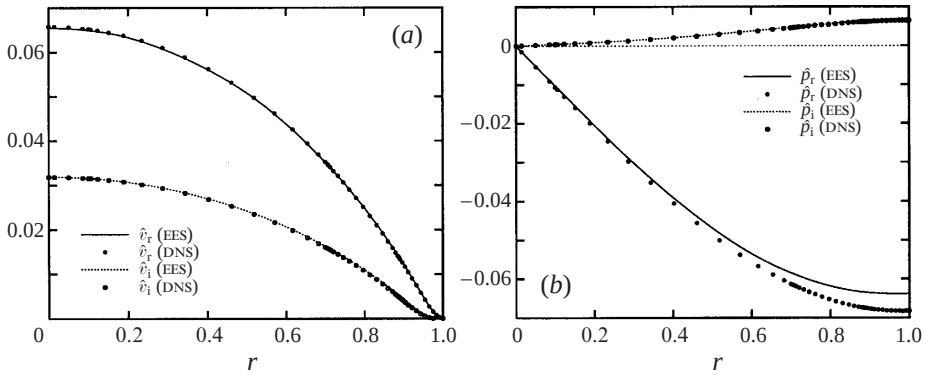

FIGURE 7. The profiles of radial velocity $\hat{v}$ and pressure $\hat{p}$ of mode $(1,1)$ at $x = -\frac{1}{2}\pi$, the left-hand edge of the PSB region ($Re = 3000, \omega = 0.5$).

In figures 6(a) and 7(a), the profiles of radial velocity $\hat{v}$ at $x = \pm\frac{1}{2}\pi$ for mode $(m,n) = (1,1)$ are shown as obtained both with the DNS and the EES. The agreement between both solution techniques is very good. A similar agreement is also found for $\hat{u}$ and $\hat{w}$ (not shown here). This agreement can be considered as a further validation of our DNS code but it has also been exploited in determining the propagation properties of the various eigenmodes as discussed in Appendix B, § B.3.

A relatively large deviation is observed, however, for the real part of pressure $\hat{p}$ (see figures 6b and 7b). To explain this fact we show the first-order x-derivative of $\hat{v}$ in figure 8(a) where a deviation between the DNS and the EES is even more apparent. The reason for this deviation is the fact that the discrete shape function $f(x)$ as applied in the DNS is non-zero outside the PSB region $x \in (-\frac{1}{2}\pi, \frac{1}{2}\pi)$ (see figure 8b). This is a consequence of the limited number of grid points which are used to represent the shape function in the DNS. As can be seen later in § 5.2, this disagreement has no significant influence on the further evolution of the disturbance.

In figure 9, we show the profiles of $\hat{v}$, $\hat{w}$ at $x = 0$ for mode $(m,n) = (1,1)$ both for the DNS results and for two eigenmode solutions based on a summation of 114 and 324 eigenmodes respectively. For the azimuthal velocity $\hat{w}$, which has a homogeneous boundary condition, the agreement between the DNS and EES is very good even with 114 eigenmodes. For the radial velocity $\hat{v}$, which has an inhomogeneous boundary

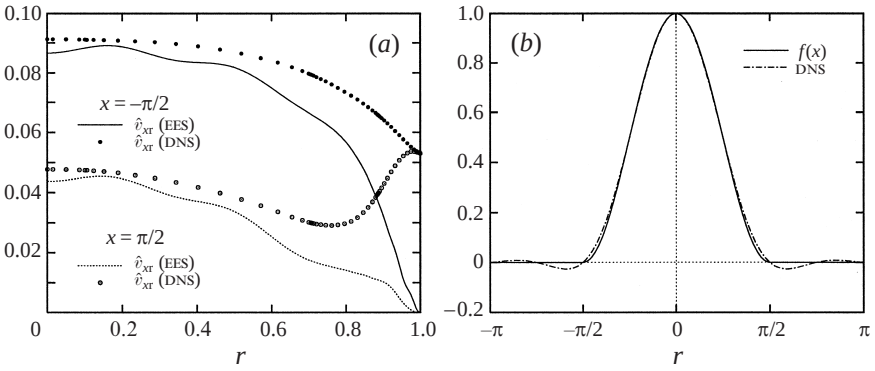

FIGURE 8. (*a*) The profiles of $\hat{v}_x$, the x-derivative of radial velocity $\hat{v}$ of mode $(1,1)$ at $x = \pm\frac{1}{2}\pi$ ($Re = 3000, \omega = 0.5$). (*b*) The shape function $f(x)$ given by (2.6) (solid line) and its approximation in the DNS (dashed-dotted line).

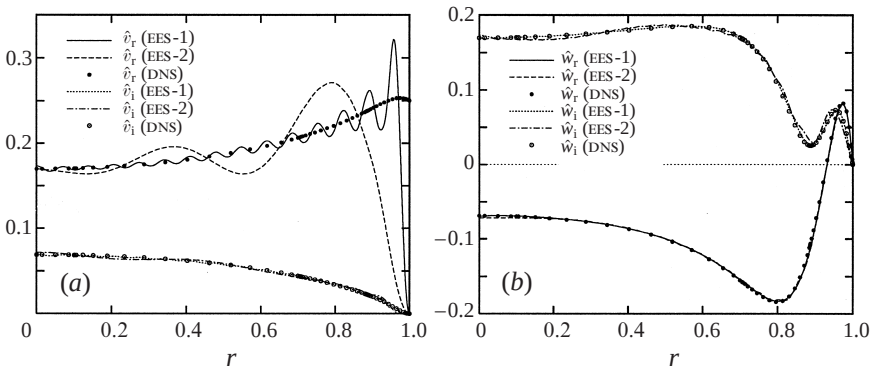

FIGURE 9. The profiles of radial and azimuthal velocities $\hat{v}$ (*a*) and $\hat{w}$ (*b*) of mode $(1,1)$ at $x = 0$, the centre of the PSB region (where EES-1 is a summation of 324 eigenmodes and EES-2 114 eigenmodes. $Re = 3000, \omega = 0.5$).

condition, the agreement is not as good. This is caused by a Gibbs phenomenon because the EES is forced to satisfy a non-zero boundary condition at $r = 1$. Fortunately, the large near-wall oscillations are found to have negligible effects on the evolution of the fundamental modes $(\pm 1, \pm 1)$ outside the PSB region. This fact has been verified by adding more eigenmodes and by comparing the results with those obtained with 324 eigenmodes. No significant difference is observed outside the PSB region. This conclusion is consistent with figure 6 where the solution is shown for $x = \frac{1}{2}\pi$ which is downstream of $x = 0$.

We shall not present here results for the harmonic modes (m_2, n_2). For these modes we cannot expect a similarly good agreement between the EES and the DNS results as for the fundamental modes (m_1, n_1), for three reasons:

1. The source term $\boldsymbol{S}_O$ in (3.11) for modes (m_2, n_2) is computed from the linear solution for the modes (m_1, n_1). It has been shown above that a fully accurate solution of modes (m_1, n_1) by means of an eigenmode expansion is not possible due to a Gibbs phenomenon for the radial velocity. Therefore, we expect the agreement between the DNS and the EES for the higher modes to be worse;

2. The DNS is actually a simulation for the full nonlinear Navier–Stokes equations and if we want a good approximation of its result by the eigenmode solu-

tion for (m_2, n_2), the following constraints must be satisfied: $|\hat{\boldsymbol{v}}(r, x; m_{3+}, n_{3+})| \ll |\hat{\boldsymbol{v}}(r, x; m_2, n_2)| \ll |\hat{\boldsymbol{v}}(r, x; m_1, n_1)| \ll 1$ (where m_{3+}, n_{3+} stand for the Fourier modes other than m_1, n_1 and m_2, n_2). Furthermore, the amplitude of the modes (m_2, n_2) should be larger than the lower bound of numerical round-off. As can be seen later in § 5.2, it is very difficult to satisfy all of these constraints simultaneously because of the large transient growth of modes $(\pm 2, 0)$;

3. The shape function $f(x)$ used in the EES and the DNS is actually different because of the numerical discretization (see figure 8*b*).

In spite of the arguments presented above, we conclude that a reasonable quantitative agreement is obtained between linear EES solution and DNS results. Therefore, both methods will be used to compute the evolution of a disturbance. In the following sections we will see that the most important features of the disturbance evolution are captured by both the EES and the DNS.

5. Results

In this section we discuss the results obtained with the eigenmode expansion solution (EES) and with the full nonlinear direct numerical simulation (DNS). We concentrate on a single PSB case with $\omega = 0.5$ as the basic disturbance frequency and $m = 1$ for the angular wavenumber. The selected Reynolds number, $Re = 3000$, in our simulation is slightly larger than the experimentally observed lower critical Reynolds number $Re_{crl} \approx 2200$.

To present our results we will use the disturbance energy which is introduced in the following subsection. The results of the computation are discussed in the two subsequent subsections. First, we consider the so-called linear regime which is characterized by a very small disturbance amplitude A_v. The downstream evolution of all dominant disturbance modes such as the (m_1, n_1) and (m_2, n_2) modes is then determined by linear processes. As pipe flow has been found to be linearly stable, all modes decay although transient growth can be quite prominent in the initial phase. Secondly we consider the results when the disturbance amplitude is increased but stays subcritical. In particular we consider the case when the flow is very close to transition. Nonlinear effects beyond the self-interaction of the fundamental modes become important now. Nevertheless, the main aspects found for the linear regime seem to remain valid at least qualitatively.

5.1. *Disturbance energy* E_{dis}

We aim to study the streamwise spatial evolution of the disturbance introduced at the pipe wall by applying the boundary condition (2.5). This disturbance introduces a perturbation velocity with frequency ω and angular wavenumber $m = 1$ superposed on the basic parabolic flow (see § 5.2 and § 5.3). A measure by which to analyse the results is the kinetic energy of the disturbance velocity.

In § 3 we have seen that the disturbance velocity can be expressed in Fourier spectral space by (3.1). The contribution to the total disturbance energy due to the modes $(\pm m, \pm n)$ denoted by $E_{\mathrm{dis}}(x; m, n)$, is then given by

$$E_{\mathrm{dis}}(x; m, n) = \sum_{j=\pm m} \sum_{k=\pm n} \frac{1}{T} \int_{\tau}^{\tau+T} \int_{0}^{2\pi} \int_{0}^{1} \tfrac{1}{2} |\hat{\boldsymbol{v}}(r, x; j, k) \mathrm{e}^{\mathrm{i}(j\theta - k\omega t)}|^2 \, r \, \mathrm{d}r \, \mathrm{d}\theta \, \mathrm{d}t$$

$$= \pi \sigma_m \sum_{k=\pm n} \int_{0}^{1} |\hat{\boldsymbol{v}}(r, x; m, k)|^2 \, r \, \mathrm{d}r. \tag{5.1}$$

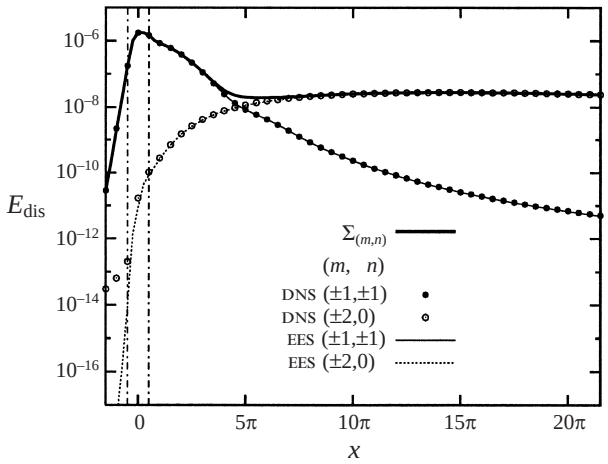

FIGURE 10. Spatial evolution of the total disturbance energy $E_{\mathrm{dis}}(x)$ and the disturbance energy for the dominant modes $(m,n) = (\pm1,\pm1)$ and $(\pm2,0)$. Two vertical '–·–·–'s delimit the PSB region. The DNS and the EES results are hardly distinguishable in most of the calculation domain and the large deviation for mode $(\pm2,0)$ at small amplitude ($E_{\mathrm{dis}} < 10^{-13}$) is mainly due to the numerical round-off of the DNS results.

Here $\sigma_m = (2 - \delta_{m0})$, $T = 2\pi/\omega$ and τ is an arbitrary starting time subject to the condition that the asymptotic temporal state has been reached. We note that this definition can only be used when there is a dominant fundamental frequency present in our flow. This means for instance that (5.1) is not useful for turbulent flows.

The disturbance energy for azimuthal mode m is then defined as the sum over all temporal modes:

$$E_{\mathrm{dis}}(x;m) = \sum_{n\geqslant 0} E_{\mathrm{dis}}(x;m,n). \tag{5.2}$$

The total disturbance energy follows as

$$E_{\mathrm{dis}}(x) = \sum_{m\geqslant 0}\sum_{n\geqslant 0} E_{\mathrm{dis}}(x;m,n). \tag{5.3}$$

This latter definition can be extended to turbulent flow by performing in that case a time average instead of the summation over modes (m,n). This extension has been applied to obtain the results shown in figure 3.

A different measure of kinetic energy concerns its temporal evolution integrated over the whole flow domain. This is defined as

$$K_{\mathrm{dis}}(t) = \iiint \tfrac{1}{2}\,|\boldsymbol{v}(x,r,\theta,t) - \boldsymbol{V}(r)|^2\, r\,\mathrm{d}x\,\mathrm{d}r\,\mathrm{d}\theta. \tag{5.4}$$

5.2. *Linear regime*

In this subsection we consider the development of a very small disturbance and in our DNS we take $A_v = 0.001$. The solution of the eigenmode expansion does not depend on a particular choice for the amplitude of the disturbance.

In figure 10 we show the evolution of the total disturbance energy and its subdivision into the fundamental modes $(\pm1,\pm1)$ and the steady harmonics $(\pm2,0)$. We find that the total energy is dominated by the fundamental modes before $x \approx 4\pi$ and by the steady harmonics after $x \approx 7\pi$. The contribution by the other modes is found to be negligible. We have argued in § 3 that the modes $(\pm2,0)$ are generated by nonlinear

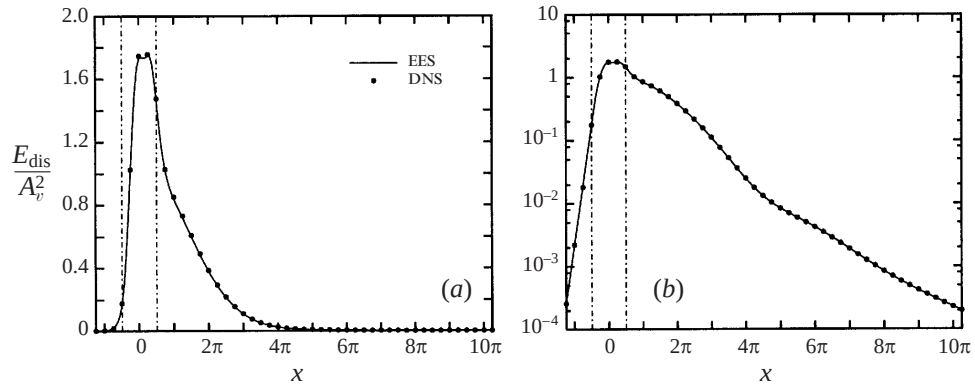

FIGURE 11. Spatial evolution of the disturbance energy $E_{dis}(x;1,1)$ ($Re = 3000, \omega = 0.5$), plotted in (a) linear and (b) logarithm coordinates.

self-interaction of the fundamental modes but in view of the fact that the further nonlinear interactions turn out to be very small, they evolve by linear processes such as transient growth and exponential decay. Therefore, we call this case the linear regime.

Let us now look at the evolution of the individual modes in more detail. In figure 11 the spatial evolution of the fundamental modes $(\pm 1, \pm 1)$ is illustrated. The excellent agreement between the EES and DNS results is apparent. We can see that the fundamental modes $(\pm 1, \pm 1)$ decay almost exponentially downstream of the PSB region. The decay rate is larger than that of the least stable eigenmode following from linear stability theory which is equal to $-2\alpha_i = 0.06630$ (see § 4.3). The reason for this is that the introduced disturbance has its largest amplitude near the pipe wall while the least stable eigenmode has its largest amplitude near the centreline of the pipe (Tumin 1996).

The behaviour of the higher harmonics (m_2, n_2) is illustrated in figure 12. For the steady harmonics $(\pm 2, 0)$ shown in figure 12(c), a large transient energy growth is observed downstream of the PSB region (note the different vertical scale). This growth lasts for a quite long distance, i.e. to $x \approx 15\pi$. In figure 10 we have already seen that as a result of this transient growth the energy of mode $(\pm 2, 0)$ becomes substantially larger than the energy of the fundamental mode. Nevertheless, the fundamental modes evolve according to a linear decay process and thus do not feel the presence of these higher harmonics. We will return to this in the next subsection when we consider higher disturbance amplitudes. For the other (m_2, n_2) modes, transient growth is also found but with a peak values three to four orders smaller than for mode $(\pm 2, 0)$ (see figure 12a, b, d).

In figure 13 we show the velocity components generated by the steady harmonics $(\pm 2, 0)$. This velocity field implies a streaky structure because the amplitude of the axial velocity $|\hat{u}|$ is two orders of magnitude larger than the other two velocity components. The presence of these streaks will be shown more clearly in the next subsection.

By means of a temporal linear analysis for optimal transient growth in Hagen–Poiseuille flow, Bergström (1993b) and Schmid & Henningson (1994) have shown that a large amplification exists for disturbances with small streamwise wavenumber $\alpha \ll 1$ and small azimuthal wavenumber m. In particular they show that modes $(m, \alpha) = (\pm 1, 0)$ have the largest amplification and modes $(\pm 2, 0)$ have the second

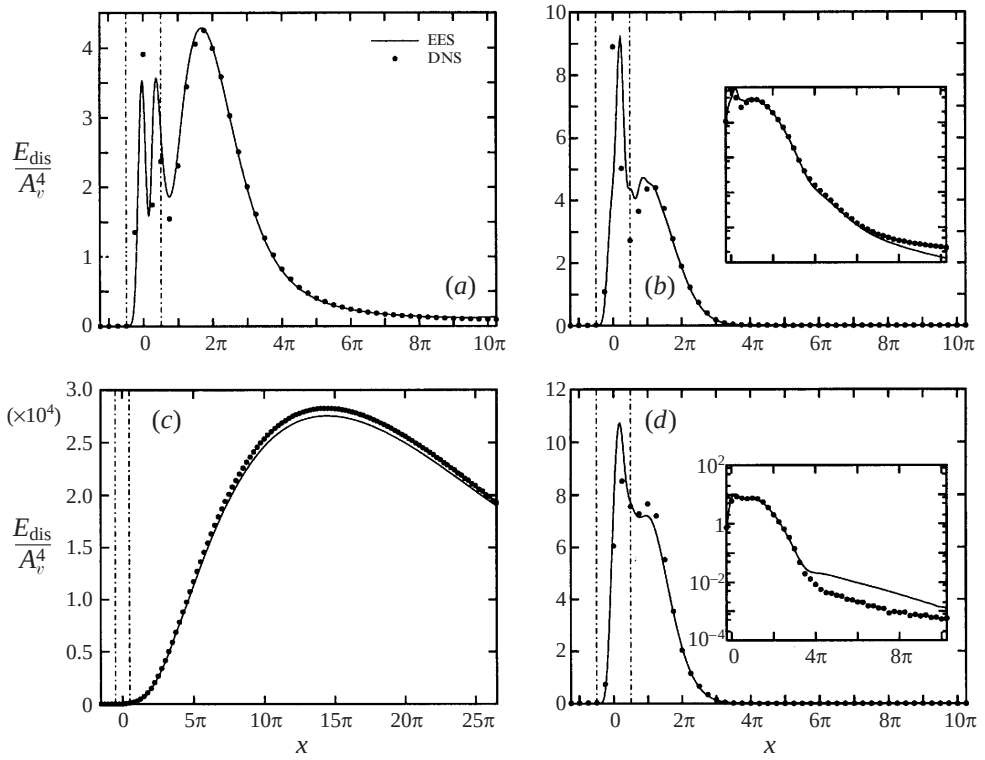

FIGURE 12. Spatial evolution of the disturbance energy for the Fourier modes which are generated from the quadratic nonlinear interaction of modes $(\pm1,\pm1)$ ($Re = 3000, \omega = 0.5$). The insets in (*b*) and (*d*) are plotted in logarithm coordinates. Note the different scale for (*c*). (*a*) $E_{\rm dis}(x;0,0)$; (*b*) $E_{\rm dis}(x;0,2)$; (*c*) $E_{\rm dis}(x;2,0)$; (*d*) $E_{\rm dis}(x;2,2)$.

largest. However, the modes $(\pm2,0)$ show almost up to their maximum a larger growth rate than the modes $(\pm1,0)$. These results for the temporal analysis seem consistent with our spatial simulation because in both cases it appears that a streaky structure (manifested by a small streamwise wavenumber α) has the largest potential for transient growth. Another confirmation of this result is given by Lundbladh *et al.* (1994) who discuss a spatial simulation for the evolution of a pair of oblique waves $(\beta,\pm\omega)$ in plane Poiseuille flow where β denotes the spanwise wavenumber. They also find large transient growth for the steady harmonic $(2\beta,0)$.

5.3. *Nonlinear regime*

When the disturbance amplitude A_v becomes large, nonlinear interaction is no longer negligible. Nevertheless, for a moderate disturbance amplitude, the flow remains laminar and exhibits a periodic behaviour in response to the imposed disturbance. This is shown in figure 14 where the periodic behaviour is clearly illustrated by the inset. Let us now consider how the most important modes, i.e. $(\pm1,\pm1)$, $(\pm2,0)$ and $(0,0)$, behave for various disturbance amplitudes: $A_v = 0.015, 0.025, 0.031, 0.0325$.

In figure 15(*a*), we show the evolution of the disturbance energy for the fundamental modes $(\pm1,\pm1)$. For these fundamental modes the deviation from the EES becomes more and more prominent as A_v increases. Apart from the peak in the disturbance region, we find additional energy peaks as A_v increases. Nevertheless, for all disturbance amplitudes the $(\pm1,\pm1)$ modes eventually decay.

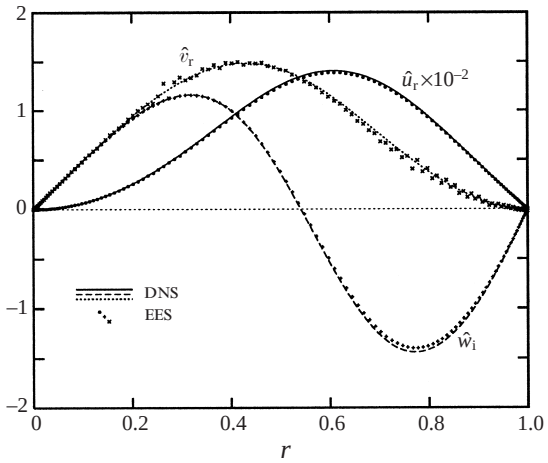

FIGURE 13. The profiles of steamwise, radial and azimuthal velocities $\hat{u}(x,r;2,0)$, $\hat{v}(x,r;2,0)$, $\hat{w}(x,r;2,0)$ at $x = 15\pi$ ($Re = 3000, \omega = 0.5$). $\hat{u}_i = \hat{v}_i = \hat{w}_r = 0$ and are not plotted. The velocity is normalized by A_v^2.

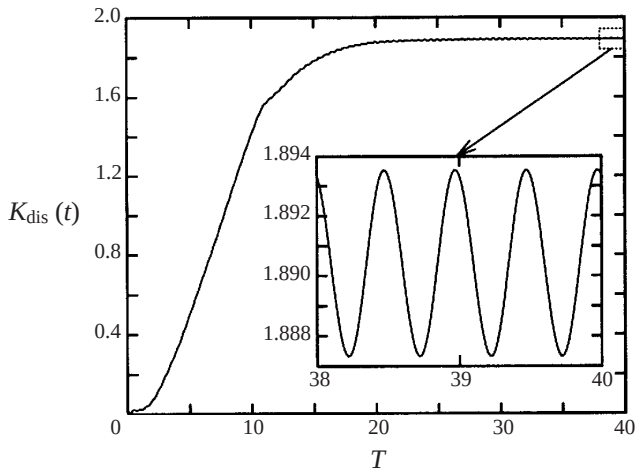

FIGURE 14. Temporal evolution of the total disturbance energy $K_{dis}(t)$ with a disturbance amplitude $A_v = 0.03$ ($Re = 3000, \omega = 0.5$). $T = 2\pi/\omega$ is the disturbance period.

Next we consider the steady harmonics $(\pm 2, 0)$ for which we have found a large transient growth in the previous subsection. The results for various amplitudes A_v are shown in figure 15(b). Here we find a similar growth but the peak value of $E_{dis}(x;2,0)$ becomes smaller as A_v increases. This must be due to nonlinear interactions and is consistent with the temporal analogue discussed by O'Sullivan & Breuer (1994b) and by Bergström (1995a) for the transient behaviour of disturbance with finite amplitude.

Although both the modes $(\pm 1, \pm 1)$ and $(\pm 2, 0)$ deviate from the linear EES results, the qualitative features are still similar. For the mean perturbation mode, $(0,0)$, the situation is different. This can be seen by comparing figure 12(a) with figure 15(c). Since the steady harmonics $(\pm 2, 0)$ are the dominant modes (see figure 16), we suspect that the growth of the mode $(0,0)$ is mainly due to the contribution of the quadratic

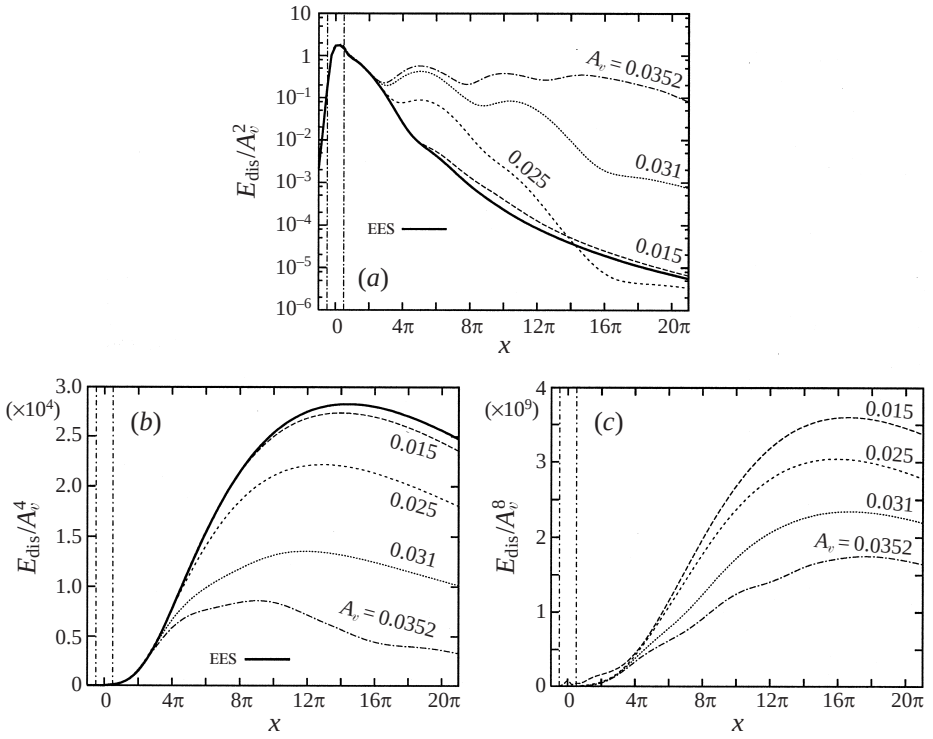

FIGURE 15. Spatial evolution of the disturbance energy ($Re = 3000, \omega = 0.5$): (*a*) $E_{dis}(x;1,1)$; (*b*) $E_{dis}(x;2,0)$; (*c*) $E_{dis}(x;0,0)$. Note the different scales for (*b*) and (*c*).

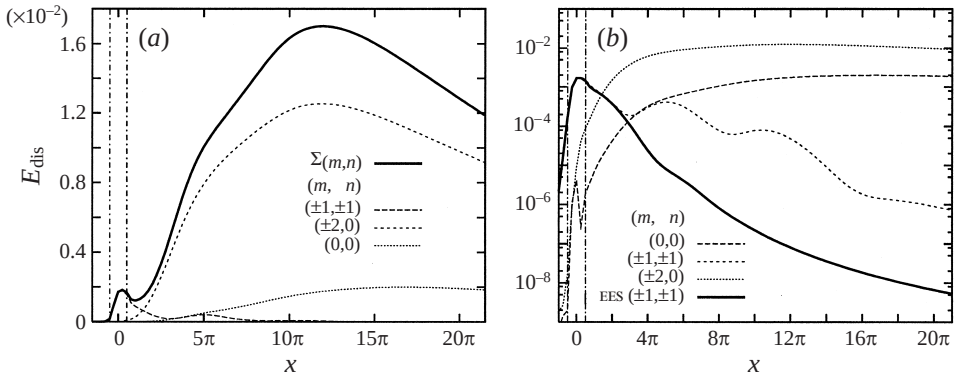

FIGURE 16. Spatial evolution of the total disturbance energy $E_{dis}(x)$ and the disturbance energy for the dominant modes $(m,n) = (\pm1,\pm1)$, $(\pm2,0)$ and $(0,0)$. The disturbance amplitude is $A_v = 0.031$. The –·–· delimit the PSB region.

self-interaction of the steady harmonics $(\pm2,0)$. Consequently the $E_{dis}(x;0,0)$ has been scaled by the eighth power of the amplitude A_v in figure 15(*c*).

In figure 16 we show the disturbance energy for the modes $(\pm1,\pm1)$, $(\pm2,0)$ and $(0,0)$ for the case of amplitude $A_v = 0.031$. At the end of the domain the total disturbance energy is determined by the steady harmonics $(\pm2,0)$ and mean perturbation mode $(0,0)$ only. Considering the decay rates of these two modes one may assume that further downstream only mode $(0,0)$ will survive. As also mentioned

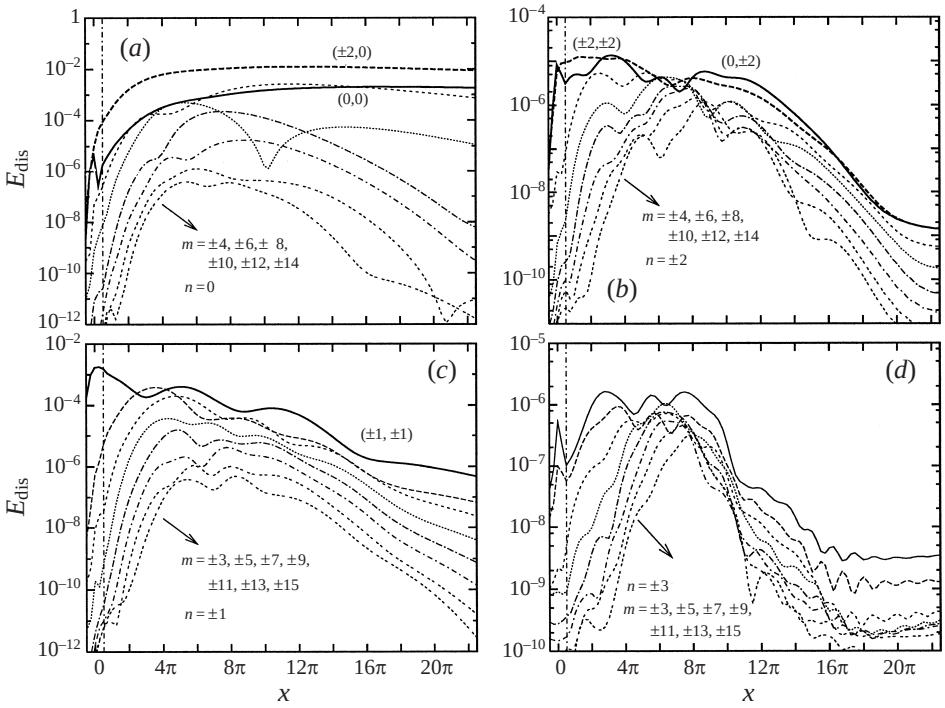

FIGURE 17. Spatial evolution of the disturbance energy for various modes. The (m_1, n_1) and (m_2, n_2) modes are shown by thick lines and marked separately. The disturbance amplitude is $A_v = 0.031$.

in the previous subsection we find that the modes $(\pm 1, \pm 1)$ seem not sensitive to the steady harmonics $(\pm 2, 0)$. The deviation of the modes $(\pm 1, \pm 1)$ from the EES results as shown in figure 15(a) should therefore be contributed to the interaction with mode $(0, 0)$ and with higher-order harmonics beyond the $(\pm 2, 0)$ modes.

In the remainder of this subsection we will show some detailed results for the two largest amplitudes $A_v = 0.031$ and 0.0325 which exhibit some prominent nonlinear features.

It is not difficult to show by means of the computational results that only the spectral groups (m, n) for which both m and n are even or for which both m and n are odd can exhibit a large disturbance energy. For these groups we show in figures 17 and 18 the disturbance energy for $A_v = 0.031$ and 0.0325, respectively. We find from these figures that the disturbance energy for modes with low frequency ($n = 0, 1$) is two or three orders larger than modes with high frequency ($n = 2, 3$). This feature is similar to that found in the β-cascade discussed by Henningson, Lundbladh & Johansson (1993) in their study on the bypass transition in plane Poiseuille flow. In analogy we shall use here the term m-cascade. In the m-cascade, the disturbance energy is mainly transferred through a route with increasing azimuthal wavenumber m, according to

$$(\pm 1, \pm 1) \Rightarrow (\pm 2, 0) \Rightarrow (\pm 3, \pm 1) \Rightarrow (\pm 4, 0) \Rightarrow \cdots .$$

We also find from figures 17 and 18 that within the m-cascade the modes with $n = 0$, such as $(\pm 2, 0), (\pm 4, 0), (\pm 6, 0)$, etc., have a large transient growth. For instance, in figure 17(a) mode $(\pm 4, 0)$ appears to be the second largest mode.

From figures 17 and 18 we can also discern a different evolution for $A_v = 0.031$ and

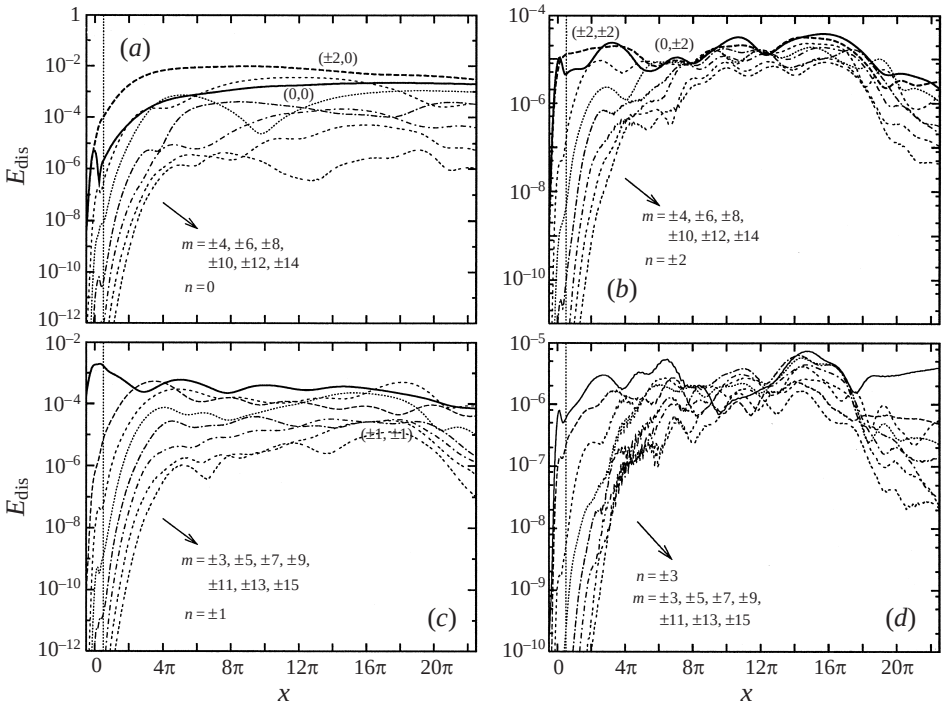

FIGURE 18. Same as figure 17 for a different disturbance amplitude $A_v = 0.0325$.

0.0325. For the smaller amplitude, most of the disturbance modes show a transient growth followed by an exponential decay as soon as the energy peak is reached. For the larger amplitude, the energy growth lasts for a longer distance. After the energy peak has been reached the modes evolve at nearly a constant energy level and smaller scale modes appear to become more important. For instance, 18(*a*) shows that mode $(\pm 6, 0)$ becomes larger than mode $(\pm 4, 0)$ at the end of the computational domain. This behaviour of the modes implies that the disturbance is nearly self-sustainable, a basic feature of turbulence. As a result, we believe $A_v = 0.0325$ is close to the critical amplitude.

We have mentioned in the previous subsection that the characteristic feature of the steady harmonics $(\pm 2, 0)$ is the generation of low-speed streaks which are defined as areas where the local streamwise velocity is smaller than the average velocity: $\tilde{u} = u - U < 0$. The generation of these streamwise streaks is caused by a so-called 'lift-up' mechanism (Landahl 1975) which results from a flow redistribution caused by travelling vortex pairs. These vortex pairs, which in our case are generated by the PSB disturbance, are illustrated in figure 19(*a*). Here we see that the vortex pairs alternate along the upper and lower walls in the streamwise direction which reflects that vortex pairs are formed only during the blowing phase of the imposed disturbance. In figure 19(*b*) the associated streamwise streaks are shown.

As follows from figure 20 there is a clear difference in development of the low-speed streaks for the two amplitudes $A_v = 0.031$ and $A_v = 0.0325$. In the former case the low-speed streaks are highly elongated in the streamwise direction and keep a nearly constant level until the end of our calculation domain is reached (see figure 20*a*). For $A_v = 0.0325$, however, the low-speed streaks no longer keep a constant level but seem to decay in the streamwise direction, while at the same time some smaller scale

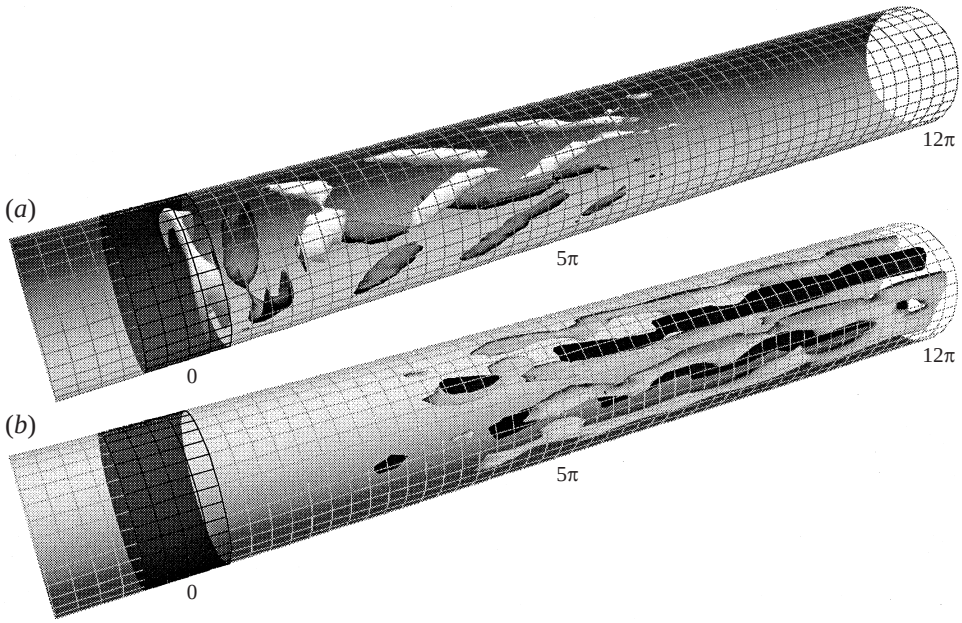

FIGURE 19. Instantaneous vortices and streamwise streaks at $t = 26T$. The disturbance amplitude $A_v = 0.031$. (*a*) Perspective view of vortex pairs, represented by the isosurface of $Q = 0.015$, where Q is the second invariant of $\nabla \boldsymbol{v}$ (see Sandham & Kleiser 1992). In the selected domain $Q_{\max} \approx 0.064$. The PSB region is located in the dark section at the left side of the pipe wall. The light and dark grey colours of the isosurfaces indicate the vortices which are generated from different sides of the PSB region; (*b*) Perspective view of streamwise streaks $\tilde{u} = u - U$, represented by the isosurfaces of $\tilde{u} = 0.1$ (light) and -0.2 (dark). In the selected domain $\tilde{u}_{\max} \approx 0.146$, $\tilde{u}_{\min} \approx -0.303$.

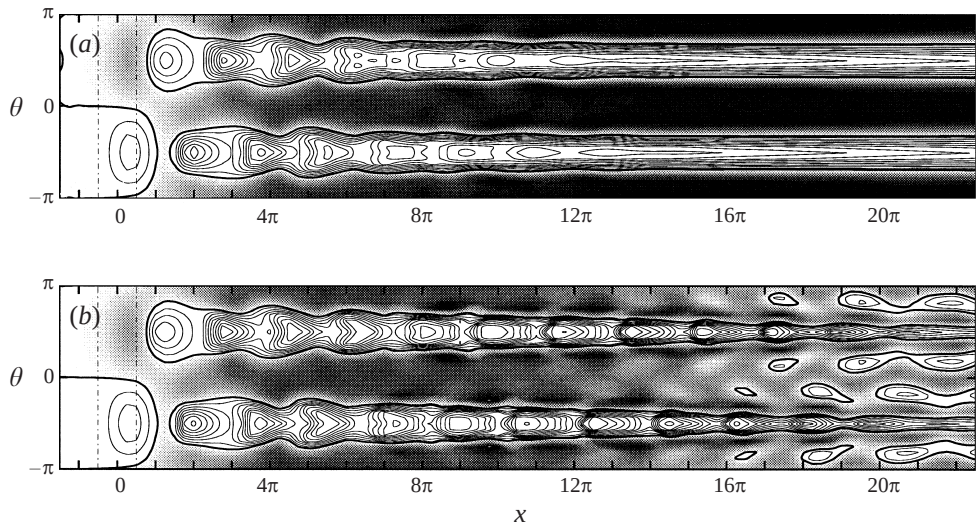

FIGURE 20. Instantaneous streamwise streaks $\tilde{u} = u - U$ at $t = 26T$ with $T = 2\pi/\omega$ the disturbance period, shown in an x, θ cross-section at $r = 0.6$, contour shading ranges from 0 (brightest) to 0.13 (darkest); contour lines range from -0.26 to 0 and spaced by 0.025. The disturbance amplitude is: (*a*) $A_v = 0.031$; (*b*) $A_v = 0.0325$.

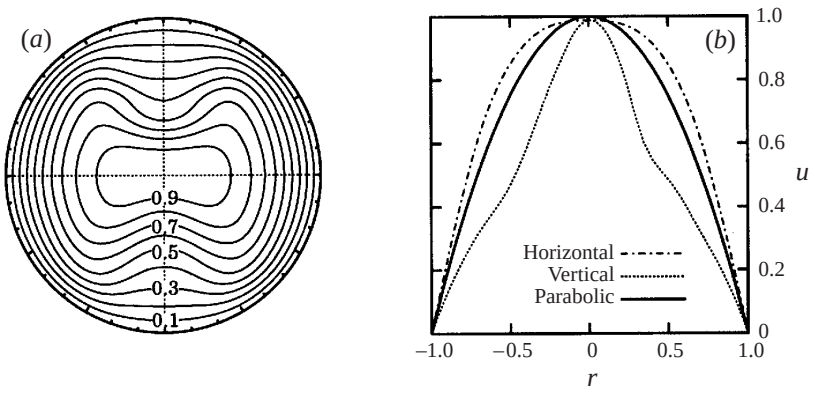

FIGURE 21. Instantaneous streamwise velocity u at $t = 26T$ for $A_v = 0.031$. (*a*) Contours in a transverse section at $x = 12\pi$; (*b*) profiles for the two cross-sections in (*a*).

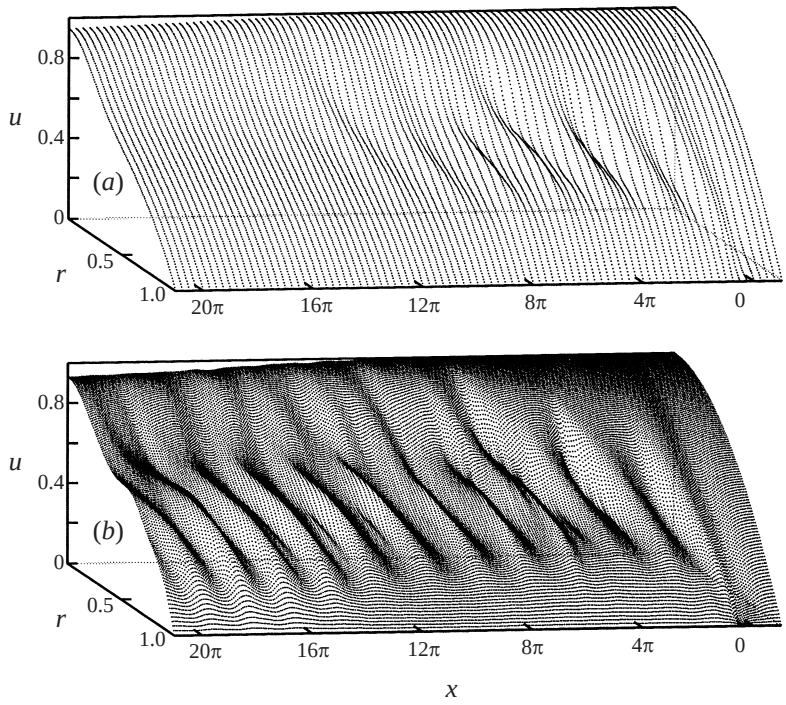

FIGURE 22. Streamwise evolution of the profiles of instantaneous streamwise velocity u at $t = 26T$ and $\theta = \frac{1}{2}\pi$. The disturbance amplitude is: (*a*) $A_v = 0.031$; (*b*) $A_v = 0.0325$.

structures in the form of streak oscillations appear as a consequence of the energy *m*-cascade (see figure 20*b*).

The main contribution of these streamwise streaks is to modulate the basic flow and the resulting instantaneous flow profile is highly distorted, exhibiting both azimuthal and radial inflection points as shown in figure 21 and figure 22. Such a modulated velocity field has been studied by Zikanov (1996) who found this flow to be highly unstable to three-dimensional disturbances.

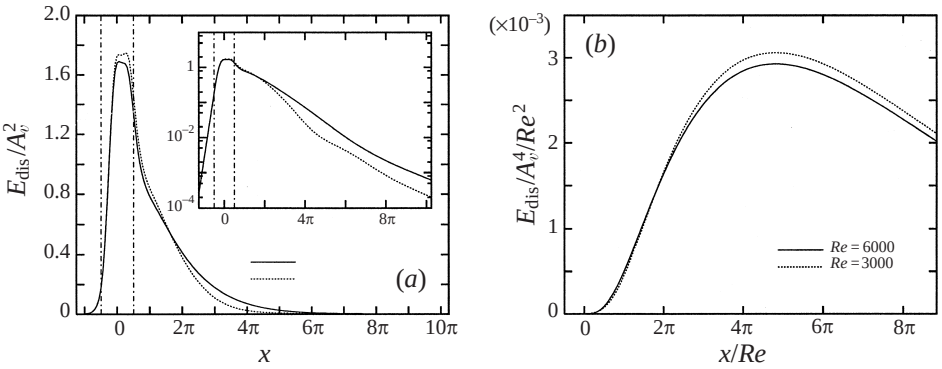

FIGURE 23. Spatial evolution of the disturbance energy for $Re = 3000$ and 6000 ($\omega = 0.5$): (*a*) $E_{\mathrm{dis}}(x; 1, 1)$; (*b*) $E_{\mathrm{dis}}(x; 2, 0)$. The –·– delimit the PSB region.

6. Discussion on parameter dependence

For natural transition, the Reynolds number Re is the only independent parameter, but for the case of triggered transition there are more independent parameters which in our situation are the disturbance frequency ω, the disturbance amplitude A_v, the disturbance azimuthal wavenumber m, the disturbance shape function $f(x)$ and the width of the disturbance region d. Dauchot & Manneville (1997) argue that when one parameter is varied while the others are kept fixed, a special path in phase space is selected towards the final transition. If a 'wrong' path is selected, the transition will never occur. So it seems pertinent to study triggered transition as a function of various parameter groups. In our numerical simulation presented in the previous section we have only considered the dependence on the disturbance amplitude A_v for a disturbance with $Re = 3000$, $\omega = 0.5$, $m = 1$, $d = \pi$ and $f(x)$ as given in (2.6). The reason for this choice was to mimic the experimental situation of Draad *et al.* (1998) where the dependence on the disturbance amplitude was carefully studied for a PSB disturbance with azimuthal wavenumber $m = 1$. The experimental situation of Eliahou *et al.* (1998) is similar but for a PSB disturbance with $m = 2$.

Let us now consider the dependence on some of these disturbance parameters. For this we restrict ourselves to results obtained with the EES technique. In principle these results are only applicable for an infinitesimal disturbance amplitude, i.e. $A_v \ll 1$. However, they can also serve as some indication on what to expect in numerical and experimental studies at larger finite disturbance amplitudes.

Reynolds number Re

To study the effect of the Reynolds number we have computed the case for $Re = 6000$. The results for the disturbance energy are shown in comparison with the results for $Re = 3000$ in figure 23. There is no significant change in the behaviour of the fundamental mode $(m, n) = (\pm 1, \pm 1)$ for both cases. On the other hand, the results for the steady harmonic $(\pm 2, 0)$ show that the peak value of the disturbance energy scales with Re^2 and its position with Re. This result suggests that for the case that transition depends only on the existence of transient growth of the steady harmonics $(\pm 2, 0)$, the critical disturbance amplitude $A_{v_{\mathrm{cr}}}$ becomes inversely proportional to Reynolds number Re. This conclusion is qualitatively similar to the experimental results obtained by Draad *et al.* (1998) who also find a Re^{-1} dependence for the critical amplitude in some range of the disturbance frequency ω. However, one should

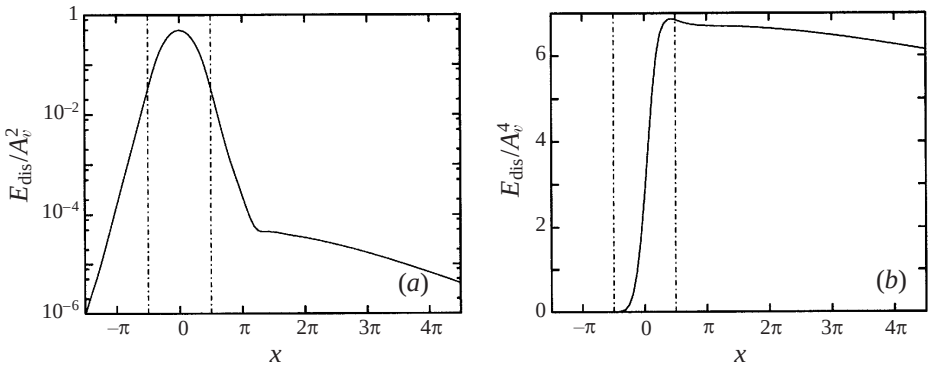

FIGURE 24. Spatial evolution of the disturbance energy for $\omega = 2.5$ ($Re = 3000$): (*a*) $E_{\rm dis}(x;1,1)$; (*b*) $E_{\rm dis}(x;2,0)$.

note again that this conclusion has been obtained with the EES approach which in principle is only valid for small disturbance amplitudes whereas the behaviour of $A_{v_{\rm cr}}$ will most likely be also influenced by nonlinear interactions.

In a linear temporal analysis Bergström (1992) found that the transient energy amplification is proportional to Re^2 for the most amplified modes (the modes for which the streamwise wavenumber $\alpha = 0$). Our conclusion thus seems analogous to these temporal results.

These results for the dependence of transition on Reynolds number also imply that a numerical study will be quite difficult for a higher Reynolds number. Namely, a longer pipe is needed for the numerical simulation since the transition position lies farther downstream. At the same time, a higher Reynolds number demands higher spatial resolution. The computational resources required for such simulation will thus become extremely large and not feasible for even the most powerful supercomputers available nowadays.

Disturbance frequency ω

In figure 24, the results for the disturbance energy are shown as obtained with a higher disturbance frequency, i.e. $\omega = 2.5$ as compared with the original value $\omega = 0.5$.

For the fundamental mode $(\pm 1, \pm 1)$ illustrated in figure 24(*a*), we find a very strong decay immediate downstream of the PSB region and then a nearly discontinuous change to a smaller decay rate. This behaviour is quite different from the results for $\omega = 0.5$ as shown in figure 11(*b*) where the decay just after the disturbance region is much slower.

For the steady harmonic $(\pm 2, 0)$ given in figure 24(*b*), the results for $\omega = 0.5$ and 2.5 are also quite different. Almost no transient growth is found for the case $\omega = 2.5$ and as a result the peak value of this mode is four orders of magnitude smaller than for $\omega = 0.5$. This result seems also consistent with the temporal linear analysis for the transient growth discussed by Bergström (1993*b*) who obtained the result that amplification of the initial disturbance energy will occur only for streamwise wavenumber $\alpha \ll 1$ for which the spatial analogue is $\omega \ll 1$ (the numerical simulation of Lundbladh *et al.* 1994 showed such an analogy to be valid for plane Poiseuille flow).

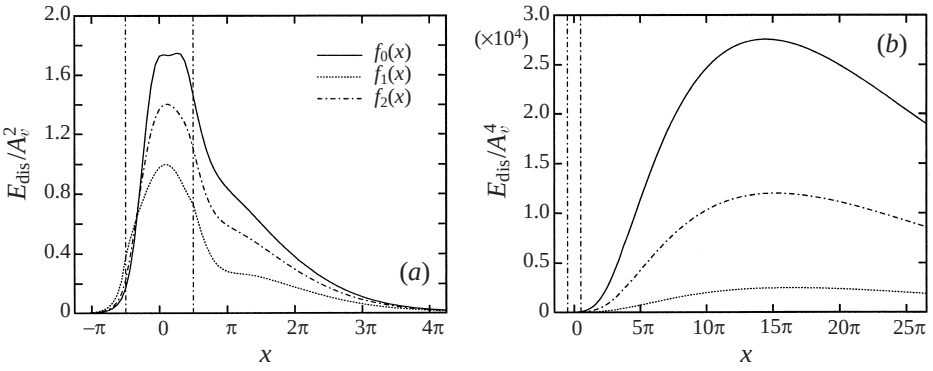

FIGURE 25. Spatial evolution of the disturbance energy for different shape functions: (*a*) $E_{dis}(x;1,1)$; (*b*) $E_{dis}(x;2,0)$. The width of PSB region is $d=\pi$ ($Re=3000, \omega=0.5$).

Shape function $f(x)$ and width of the slit d

Next we consider the influence of the shape function on the evolution of the flow. It is very difficult in an experiment to accurately measure the disturbance shape function $f(x)$. One can perhaps estimate $f(x)$ to lie in between the solution with free slip and no-slip boundary conditions in the slit. The former leads to a constant step function given by

$$f_1(x)=\tfrac{1}{2},$$

and the latter is the parabolic profile given by

$$f_2(x)=\frac{3}{4}\left(1-\frac{4x^2}{d^2}\right).$$

The choice for the subscripts is based on the convention that we denote the numerical shape function (2.6) as $f_0(x)$. We note again that $f_0(x)$ is not based on a physical argument but its C^1 continuity is required to suppress the Gibbs phenomenon of the spectral method used in our simulation. The amplitude of the three shape functions have been adjusted such that the same mass flux is entering and leaving through the pipe wall during each period, i.e. their integral across the slit is normalized to unity.

In figure 25 we show the results for the disturbance energy obtained with the three shape functions. The total disturbance energy depends on the square of these shape functions integrated across the slit. It is not difficult to show that this integral is smallest for $f_1(x)$. This fact explains why we find the lowest values for $E_{dis}(x;1,1)$ and $E_{dis}(x;2,0)$ for shape function $f_1(x)$. The original shape function (2.6) has the largest energy. These results also support the hypothesis of Eliahou *et al.* (1998) who ascribe the discrepancy between their experimental and theoretical results to a possible difference between the experimental and theoretical shape functions.

These results for the dependence on the disturbance shape have been obtained for a slit with a width of $d=\pi$. In the experiments of both Eliahou *et al.* (1998) and Draad *et al.* (1998) the PSB region is much more narrow, i.e. $d=0.1212$ in the case of Eliahou *et al.* (1998) and $d=0.0275$ for Draad *et al.* (1998). By means of the EES method it is possible to explore the dependence of the solution on the width d whereas this would have been nearly impossible for a full nonlinear DNS due to resolution requirements.

The results obtained with the EES method for the same three shape functions as discussed above but now for the width $d=0.0275$ are shown in figure 26 (the shape of

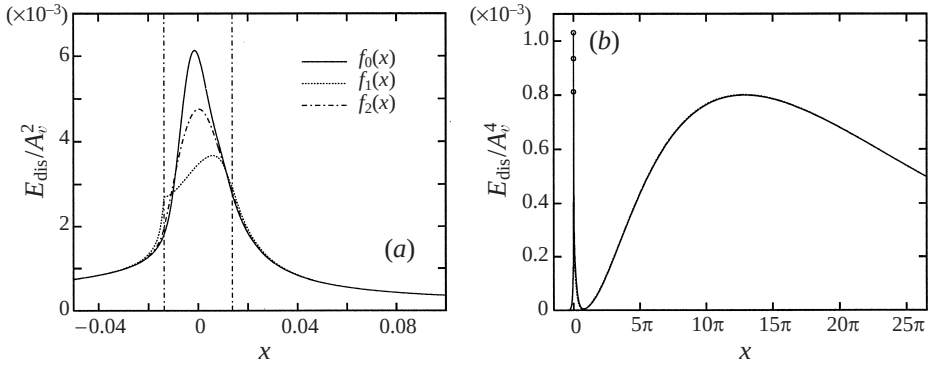

FIGURE 26. Spatial evolution of the disturbance energy for different shape functions: (*a*) $E_{\mathrm{dis}}(x;1,1)$; (*b*) $E_{\mathrm{dis}}(x;2,0)$. The peak values of $E_{\mathrm{dis}}(x;2,0)$ for different shape functions are denoted as small circles, and correspond to f_0, f_2 and f_1 from the largest one to the smallest. The width of PSB region is $d = 0.0275$ ($Re = 3000, \omega = 0.5$).

the solution for $d = 0.1212$ is nearly the same apart from a slightly different amplitude and therefore not shown here). In this case the variation in the disturbance energy between different shape functions is restricted to the PSB region and its immediate vicinity. Further downstream of the PSB region the behaviour of E_{dis} as function of x is nearly the same for all cases. Therefore, we believe that for the experiments the evolution of the disturbance should be quite insensitive to the details of the disturbance shape.

We can estimate the total disturbance energy $E_{\mathrm{dis}}(x)$ from a summation of $E_{\mathrm{dis}}(x;1,1)$ and $E_{\mathrm{dis}}(x;2,0)$. The results following from figure 25 for $d = \pi$ then imply that for $A_v < 1$ the peak value of $E_{\mathrm{dis}}(x)$ is determined by transient growth and located far from the PSB region. On the other hand for $d = 0.0275$ the peak value of $E_{\mathrm{dis}}(x)$ is not determined by transient growth as follows from figure 26 and it is located inside the PSB region. So in the experiments of Eliahou *et al.* (1998) and Draad *et al.* (1998), transient growth may be not as important as in our numerical simulation.

7. Conclusion

With help of a full nonlinear direct numerical simulation based on a spectral element model and of an eigenmode expansion solution, we have investigated the spatial evolution of a disturbance imposed on Hagen–Poiseuille flow. The perturbation is introduced in the flow by periodic suction and blowing through a narrow slit in the pipe wall. To mimic the recent experiments of Draad *et al.* (1998), we have limited ourselves to a disturbance with angular wavenumber $m = 1$. The frequency of the periodic suction and blowing has been set equal to $\omega = 0.5$. The amplitude of the disturbance A_v has been kept subcritical which means that no transition to turbulence occurs. In particular we have tried to obtain results near the critical amplitude, i.e. just before the flow becomes turbulent.

Based on these computational results we propose a transition scenario which is illustrated in figure 27. The flow behaviour is described in terms of so-called flow modes which are denoted by the number pair (m,n). The mode $(\pm 1, \pm 1)$ has the same angular wavenumber and frequency as the imposed disturbance, i.e $m = 1$ and $\omega = 1 \times 0.5$. It is therefore called the fundamental mode. The most important higher-order modes turn out to be: first, $(\pm 2, 0)$, which has twice the angular wavenumber

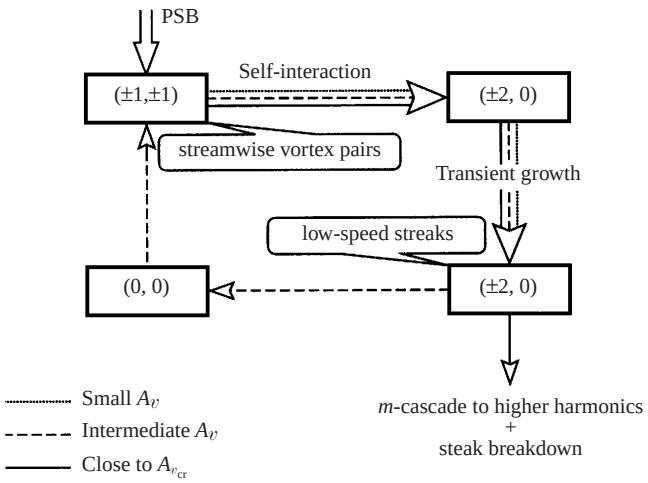

FIGURE 27. An illustration of the transition scenario in a cylindrical pipe as suggested by the investigation carried out in this paper.

of the disturbance and zero frequency and which is called the steady harmonic; and second, $(0, 0)$, which is called the mean flow perturbation.

The following three cases based on the value of the disturbance amplitude can be distinguished.

1. A_v very small. The fundamental mode (after being excited) decays exponentially as a result of a linear process. The steady harmonic after being excited by self-interaction of the fundamental mode grows at first strongly as a result of transient growth which itself is a linear process. After a maximum disturbance energy has been reached, this steady harmonic also starts to decay exponentially.

2. A_v intermediate. The behaviour of the fundamental and steady harmonic is quite similar to the case for A_v small, apart from the fact that transient growth is not as strong. The transient growth results in strong (steady) low-speed streaks in the streamwise velocity. The steady harmonic generates through self-interaction the mean flow perturbation which then starts to influence the fundamental mode.

3. A_v near critical. Also here the initial phase of evolution of the fundamental and steady harmonics up to the generation of low-speed streaks is the same as for intermediate A_v. In this case, however, many higher-order modes are excited through a so-called *m*-cascade. The result is that the low-speed streaks exhibit small-scale oscillations.

It is known that as a result of a low-speed streak inflection points appear on the instantaneous streamwise velocity. These are known to be highly unstable and the small-scale oscillations found the near critical A_v appear to be the first sign of this instability. We therefore expect the flow to become turbulent for only a very small increase of the disturbance amplitude for this case.

With help of the eigenmode expansion solution we have also considered the influence of various flow and disturbance parameters. Based on the results obtained for a higher Reynolds number we find that the critical amplitude for the transition scenario discussed above scales as Re^{-1}. For computations with a larger disturbance frequency and with a more narrow slit we find that transient growth becomes small. This implies that the critical amplitude in these cases must be larger than when

$m = 0$	$\breve{u}' = \breve{v} = \breve{w} = \breve{p} = 0$
$\lvert m\rvert = 1$	$\breve{u} = \breve{v}' = \breve{w}' = \breve{p} = 0, \quad \breve{v} + \mathrm{i}m\breve{w} = 0$
$\lvert m\rvert = 2$	$\breve{u} = \breve{v} = \breve{w} = \breve{p} = 0, \quad \breve{u}' = 2\breve{v}' + \mathrm{i}m\breve{w}' = 0$
$\lvert m\rvert \geqslant 3$	$\breve{u} = \breve{v} = \breve{w} = \breve{p} = 0, \quad \breve{u}' = \breve{v}' = \breve{w}' = 0$

TABLE 2. Central boundary conditions for (2.3).

transient growth plays a role in the critical amplitude. This seems in agreement with the experimental data of Draad *et al.* (1998).

Our overall conclusion is that a transition scenario based on transient growth exists in cylindrical pipe flow. However, our investigation of the parameter dependence also suggests that other transition scenarios cannot be excluded. This is also indicated by the experiments of Draad *et al.* (1998) which show a scaling of the critical amplitude according to $Re^{-2/3}$ and this cannot be explained by transient growth. Other transition scenarios would be in agreement with the viewpoint of Dauchot & Manneville (1997) but the search for such scenarios is left for further study.

The authors are indebted to Dr D. S. Henningson for providing information on the fringe method. Also some discussions with Drs D. S. Henningson and P. J. Schmidt are gratefully acknowledged. We thank Dr A. Tumin for sending us preprints of his unpublished work. One of us (M. B.) has been supported by a research fellowship awarded by the Delft University of Technology. Dr M. J. B. M. Pourquié has assisted with running the code. The computer time on the Cray-J90 has been made available by the Centre for High Performance Applied Computing (HPαC) of the Delft University of Technology and time on the Cray-C90 by the national foundation for the use of supercomputers (NCF). The first and third authors would like to thank the NNSFC (Grant-19732005) and the Minsistry of Science and Technology of China for their financial support.

Appendix A. Boundary condition at $r = 0$

When spectral methods are used, the solution of (2.3) is transformed into Fourier spectral space which for the azimuthal direction implies

$$\boldsymbol{v}(x, r, \theta, t) = \sum_m \breve{\boldsymbol{v}}(x, r, t; m)\mathrm{e}^{\mathrm{i}m\theta}, \qquad p(x, r, \theta, t) = \sum_m \breve{p}(x, r, t; m)\mathrm{e}^{\mathrm{i}m\theta}. \tag{A 1}$$

The conditions to be imposed at $r = 0$ vary as function of azimuthal wavenumber m and they are given in table 2. Similar results on these conditions have been presented by O'Sullivan & Breuer (1994*a*). These authors, however, give only minimal information on how these relations are obtained. Therefore, we present in this Appendix a more detailed derivation of these centreline conditions.

As follows from (2.3), the divergence term $\nabla \cdot \boldsymbol{v}$, the pressure gradient term ∇p, the nonlinear term $\boldsymbol{v} \cdot \nabla \boldsymbol{v}$ and the Laplacian term $\nabla^2 \boldsymbol{v}$ are all singular at $r = 0$. In order to find an analytical extension, or in another words to obtain a bounded solution at $r = 0$, the singularity at $r = 0$ must be removable. To achieve this, all singular terms must have a finite limit for $r = 0$. By applying L'Hôpital's rule the following

conditions can be obtained:

$$\begin{array}{rccc}
\nabla\cdot\boldsymbol{v}<\infty\Rightarrow & v+w_\theta=0, & & \\
\nabla p<\infty\Rightarrow & p_\theta=0, & & \\
\boldsymbol{v}\cdot\nabla\boldsymbol{v}<\infty\Rightarrow & wu_\theta=0, & wv_\theta-w^2=0, & ww_\theta+vw=0, \\
\nabla^2\boldsymbol{v}<\infty\Rightarrow & u_{\theta\theta}=0, & v_{\theta\theta}-v-2w_\theta=0, & w_{\theta\theta}-w+2v_\theta=0, \\
 & u'_{\theta\theta}+u'=0, & v'_{\theta\theta}-2w'_\theta=0, & w'_{\theta\theta}+2v'_\theta=0.
\end{array}$$

Here we have used the subscripts θ and $\theta\theta$ to denote the first- and second-order derivatives with respect to θ and a prime $'$ to denote the first-order derivative with respect to r.

By applying (A 1), the above conditions can be transformed into Fourier spectral space and be simplified as

$$\begin{array}{rcrcl}
\nabla\cdot\boldsymbol{v}<\infty\Rightarrow & \check{v}+\mathrm{i}m\check{w} & = & 0, & \\
\nabla p<\infty\Rightarrow & \mathrm{i}m\check{p} & = 0 \Rightarrow & \check{p}=0 & \text{when } m\neq 0, \\
\nabla^2\boldsymbol{v}<\infty\Rightarrow & -m^2\check{u} & = 0 \Rightarrow & \check{u}=0 & \text{when } m\neq 0, \\
 & -(m^2-1)\check{u}' & = 0 \Rightarrow & \check{u}'=0 & \text{when } |m|\neq 1, \\
 & -(m^2+1)\check{v}-2\mathrm{i}m\check{w} & = 0 & \check{v}=\check{w}=0 & \text{when } |m|\neq 1, \\
 & -(m^2+1)\check{w}+2\mathrm{i}m\check{v} & = 0 \Rightarrow & \check{v}+\mathrm{i}m\check{w}=0 & \text{when } |m|=1, \\
 & -m^2\check{v}'-2\mathrm{i}m\check{w}' & = 0 & \check{v}'=\check{w}'=0 & \text{when } |m|\neq 2, \\
 & -m^2\check{w}'+2\mathrm{i}m\check{v}' & = 0 \Rightarrow & 2\check{v}'+\mathrm{i}m\check{w}'=0 & \text{when } |m|=2,
\end{array}$$

where the double prime $''$ denotes the second-order derivative with respect to r.

We still require a condition for $\check{p}$ when $m=0$. To obtain this we apply the above results to the r-momentum equation for $m=0$. The result reads

$$\check{v}_t+N_r=-\check{p}'+\frac{1}{Re}\left(\tfrac{3}{2}\check{v}''+\check{v}_{xx}\right)$$

where the subscript t denotes the first-order derivative with respect to t, xx denotes the second-order derivatives with respect to x. N_r is the nonlinear term and can be proven to be zero at $r=0$, so that with $\check{v}=0$ when $m=0$, $\check{p}'=\frac{3}{2}\check{v}''/Re$ at $r=0$. We can simplify this result further by taking the first-order r-derivative of the continuity equation with $m=0$. The result reads

$$\check{u}'_x-\frac{\check{v}}{r^2}+\frac{\check{v}'}{r}+\check{v}''=0,$$

which leads to $v''=0$. The condition at the centreline for $\check{p}$ when $m=0$ thus becomes

$$\check{p}'=0.$$

At this stage we have derived all of the conditions listed in table 2.

It is furthermore worth pointing out that the conditions obtained above are based on the linear terms only. It can be shown that the restriction for the nonlinear term $\boldsymbol{v}\cdot\nabla\boldsymbol{v}<\infty$ is automatically satisfied by applying the linear results listed in table 2. This means that our results apply both to the nonlinear and the linearized Navier–Stokes equations. The extension of the above results to problems (3.4) and (B 2) is straightforward. A similar approach can by applied to problem (B 5) and here only the final results are listed in table 3.

$m = 0$	$G'_{\alpha 1} = G_{\alpha 2} = G_{\alpha 3} = G'_{\alpha 4} = G_{\alpha 5} = G_{\alpha 6} = 0$	
$\lvert m\rvert = 1$	$G_{\alpha 1} = G'_{\alpha 2} = G'_{\alpha 3} = G_{\alpha 4} = G'_{\alpha 5} = G'_{\alpha 6} = 0,$	$G_{\alpha 2} + \mathrm{i}mG_{\alpha 3} = G_{\alpha 5} + \mathrm{i}mG_{\alpha 6} = 0$
$\lvert m\rvert = 2$	$G_{\alpha 1} = G_{\alpha 2} = G_{\alpha 3} = G_{\alpha 4} = G_{\alpha 5} = G_{\alpha 6} = 0,$	$G'_{\alpha 4} = 2G'_{\alpha 2} + \mathrm{i}mG'_{\alpha 3} = 2G'_{\alpha 5} + \mathrm{i}mG'_{\alpha 6} = 0$
$\lvert m\rvert \geqslant 3$	$G_{\alpha 1} = G_{\alpha 2} = G_{\alpha 3} = G_{\alpha 4} = G_{\alpha 5} = G_{\alpha 6} = 0,$	$G'_{\alpha 2} = G'_{\alpha 3} = G'_{\alpha 4} = G'_{\alpha 5} = G'_{\alpha 6} = 0$

TABLE 3. Central boundary conditions for (B 5).

Appendix B. Spectrum of the spatial linear evolution operator $\mathscr{L}$ for Hagen–Poiseuille flow

The spatial linear operator $\mathscr{L}$ which appears in (3.4) is a differential operator and can be written as

$$\mathscr{L}(\cdot) \equiv \sum_{k=0}^{2} \mathscr{C}_k \frac{\mathrm{d}^k(\cdot)}{\mathrm{d}r^k}, \tag{B 1}$$

where $\mathscr{C}_k (k = 0, 1, 2)$ are 6×6 coefficient matrices which take the form

$$\mathscr{C}_0 = \begin{pmatrix} 0 & -1/r & -\mathrm{i}m/r & 0 & 0 & 0 \\ 0 & 0 & 0 & 0 & 1 & 0 \\ 0 & 0 & 0 & 0 & 0 & 1 \\ m^2/r^2 - \mathrm{i}n\omega Re & -Re\,U/r + Re\,U' & -\mathrm{i}mRe\,U/r & 0 & 1/r & \mathrm{i}m/r \\ 0 & (m^2+1)/r^2 - \mathrm{i}n\omega Re & 2\mathrm{i}m/r^2 & 0 & Re\,U & 0 \\ 0 & -2\mathrm{i}m/r^2 & (m^2+1)/r^2 - \mathrm{i}n\omega Re & -\mathrm{i}m/r & 0 & Re\,U \end{pmatrix},$$

$$\mathscr{C}_1 = -\begin{pmatrix} 0 & 1 & 0 & 0 & 0 & 0 \\ 0 & 0 & 0 & 0 & 0 & 0 \\ 0 & 0 & 0 & 0 & 0 & 0 \\ 1/r & Re\,U & 0 & 0 & -1 & 0 \\ 0 & 1/r & 0 & 1 & 0 & 0 \\ 0 & 0 & 1/r & 0 & 0 & 0 \end{pmatrix}, \quad \mathscr{C}_2 = -\begin{pmatrix} 0 & 0 & 0 & 0 & 0 & 0 \\ 0 & 0 & 0 & 0 & 0 & 0 \\ 0 & 0 & 0 & 0 & 0 & 0 \\ 1 & 0 & 0 & 0 & 0 & 0 \\ 0 & 1 & 0 & 0 & 0 & 0 \\ 0 & 0 & 1 & 0 & 0 & 0 \end{pmatrix}.$$

In this Appendix, we first investigate the eigenvalue system associated with the operator $\mathscr{L}$. Then the eigenspectrum of $\mathscr{L}$ is given for the fundamental modes $(m, n) = (\pm 1, \pm 1)$, the steady harmonics $(\pm 2, 0)$ and the mean perturbation mode $(0, 0)$. The possible influence of transient growth on these modes is discussed. Finally we present a discussion on the contribution of the various eigenmodes to the evolution of the disturbance as a function of the axial coordinate x.

B.1. *Eigenvalue system*

We can write the eigenvalue system corresponding to operator $\mathscr{L}$ as

$$\mathrm{i}\alpha \boldsymbol{F}_\alpha = \mathscr{L}\boldsymbol{F}_\alpha. \tag{B 2}$$

The operator $\mathscr{L}$ is complete and its eigenvectors $\boldsymbol{F}_\alpha$ span a Hilbert space $\mathscr{H} = L^2[0, 1]$. For $\boldsymbol{F}_\alpha, \boldsymbol{F}_\beta \in \mathscr{H}$, the inner product is defined as

$$(\boldsymbol{F}_\alpha, \boldsymbol{F}_\beta) \equiv \int_0^1 r \boldsymbol{F}_\beta^\dagger \boldsymbol{F}_\alpha \, \mathrm{d}r, \tag{B 3}$$

where the superscript † denotes the Hermitian adjoint matrix. At $r = 0$, $\boldsymbol{F}_\alpha$ is bounded (see Appendix A) and at $r = 1$ it satisfies the following Dirichlet boundary conditions:

$$r = 1 : \quad \boldsymbol{F}_{\alpha 1} = \boldsymbol{F}_{\alpha 2} = \boldsymbol{F}_{\alpha 3} = 0. \tag{B 4}$$

The operator $\mathscr{L}$ is not self-adjoint, so $(\boldsymbol{F}_\alpha, \boldsymbol{F}_\beta) \neq \delta_{\alpha\beta}$. The adjoint eigenvalue system is given by

$$(\mathrm{i}\alpha)^* \boldsymbol{G}_\alpha = \mathscr{L}^* \boldsymbol{G}_\alpha, \tag{B 5}$$

where the adjoint operator $\mathscr{L}^*$ is defined as

$$\mathscr{L}^*(\cdot) \equiv \sum_{k=0}^{2} (-1)^k \frac{1}{r} \frac{\mathrm{d}^k (r\, \mathscr{C}_k^\dagger(\cdot))}{\mathrm{d}r^k}. \tag{B 6}$$

At $r = 0$, G_α is also bounded (see Appendix A, table 3) and at $r = 1$, an adjoint boundary condition should be satisfied, given by

$$r = 1: \quad G_{\alpha 4} = G_{\alpha 5} = G_{\alpha 6} = 0. \tag{B 7}$$

The orthogonality relation then becomes

$$(\boldsymbol{F}_\alpha, \boldsymbol{G}_\beta) \equiv \int_0^1 r \boldsymbol{G}_\beta^\dagger \boldsymbol{F}_\alpha \, \mathrm{d}r = \delta_{\alpha\beta}. \tag{B 8}$$

There are four independent parameters for the eigenvalue problem (B 2), (B 4) and (B 5), (B 7): the azimuthal wavenumber m, the basic frequency ω, the harmonics of the basic frequency indicated by n which denotes the harmonic $n\omega$ and the Reynolds number Re. For the basic frequency we have taken here $\omega = 0.5$ and for the Reynolds number $Re = 3000$. The eigenvalue problem for the remaining parameters (m, n) has been solved numerically by a standard Chebyshev collocation method. For $m = \pm 1$, 256 collocation points are used and for $m \neq \pm 1$, 128 collocation points. We have checked extensively that the obtained eigenvalues have indeed converged.

B.2. *Spectra of operator* $\mathscr{L}$

The spectra of $\mathscr{L}$ are sets of discrete points in complex plane. In this subsection we focus on the spectra for three important cases of the parameter group (m, n): $(m, n) = (\pm 1, \pm 1), (\pm 2, 0)$ and $(0, 0)$. We will use $\mathscr{L}_{(m,n)}$ to denote the $\mathscr{L}$ operator for mode (m, n).

Spectra for fundamental modes $(\pm 1, \pm 1)$

The mode $(m, n) = (1, 1)$ is one of the four fundamental modes $(\pm 1, \pm 1)$, with given Reynolds number Re and fundamental frequency ω. It can be shown that the eigenspectrum for $\mathscr{L}_{(-1,1)}$ is the same as for $\mathscr{L}_{(1,1)}$ (the corresponding eigenfunctions are different only in terms of the sign of the components $\hat{w}$ and $\hat{w}_x$). The eigenvalues and eigenfunctions for the operators $\mathscr{L}_{(-1,-1)}$ and $\mathscr{L}_{(1,-1)}$ are conjugate to $\mathscr{L}_{(1,1)}$ and $\mathscr{L}_{(-1,1)}$ respectively.

First we show in figure 28 an overall view of the eigenspectrum for $\mathscr{L}_{(1,1)}$. The eigenmodes in the first quadrant have been studied carefully by Tumin (1996). The eigenmodes in the other quadrants are not as well documented but we will show later in § B.3 that these eigenmodes are important to obtain correct results for the evolution of the disturbance.

Since the operator $\mathscr{L}$ is not self-adjoint, it can support transient growth of initial disturbance energy; this can be can be illustrated by the ϵ-pseudospectrum of $\mathscr{L}$. There are several equivalent definitions for the ϵ-pseudospectrum and here we use the following one: the ϵ-pseudospectrum $\Lambda_\epsilon(\mathscr{L})$ of a closed operator $\mathscr{L}$ is a set of complex numbers z which satisfies $\|z\mathscr{I} - \mathscr{L}\| \leqslant \epsilon$ with $\|\cdot\|$ the norm induced by the inner product (B 3) and $\mathscr{I}$ the unit operator. The $\Lambda_\epsilon(\mathscr{L})$ are nested and $\Lambda_0(\mathscr{L})$

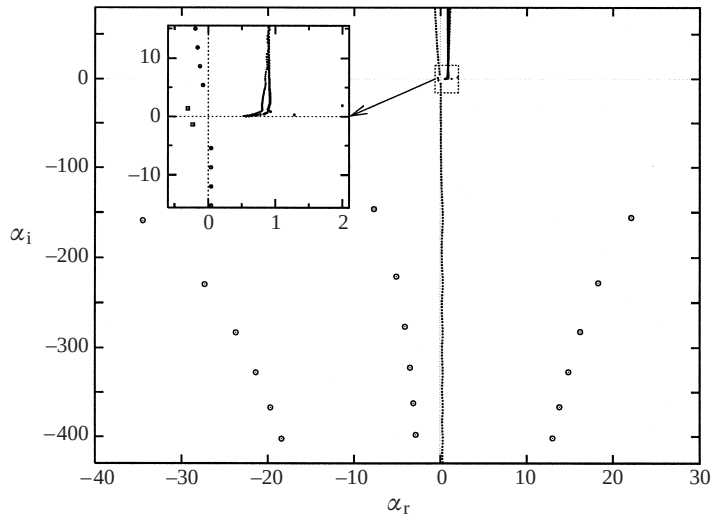

FIGURE 28. Spectrum of operator $\mathscr{L}_{(1,1)}$ for $(\omega, Re) = (0.5, 3000)$. α_r and α_i are the real and imaginary part of the eigenvalue α respectively.

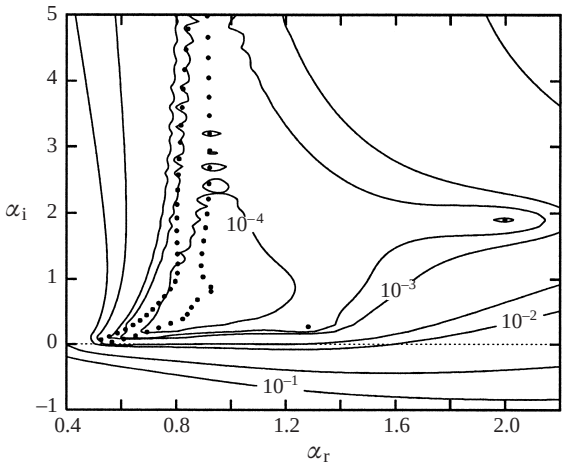

FIGURE 29. Spectrum and ϵ-pseudospectrum of $\mathscr{L}_{(1,1)}$ for $(\omega, Re) = (0.5, 3000)$. The small dots $\cdot$ represent the spectrum and the contour lines represent the outer boundaries of the ϵ-pseudospectrum where the values of the contour lines give the ϵ.

is actually the eigenspectrum of $\mathscr{L}$. Transient energy growth is possible when there exists at least one ϵ for which $\Lambda_\epsilon(\mathscr{L})$ extends to the unstable half-plane and satisfies inequality†

$$\gamma_\epsilon \equiv \sup_{\epsilon \geqslant 0} \frac{|\beta(\epsilon)|}{\epsilon} > 1,$$

where $\beta(\epsilon)$ is the minimum of the imaginary part of $\Lambda_\epsilon(\mathscr{L})$.

In figure 29 the ϵ-pseudospectrum of $\mathscr{L}_{(1,1)}$ is shown. We have restricted ourselves to show only a part of the first quadrant because the pseudospectrum in the other

† Note that the *energy* here associated with the norm $\|\cdot\|$ is different from the energy E_{dis} introduced in § 5.1, but both of them can indicate the growth of a disturbance.

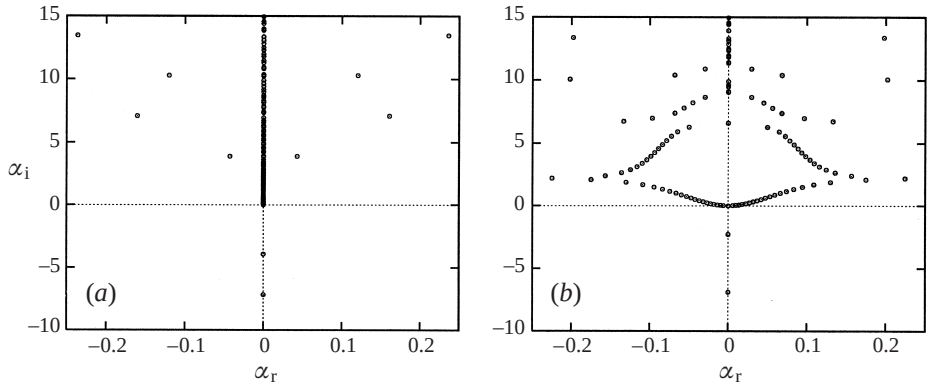

FIGURE 30. Spectrum of operator $\mathscr{L}_{(0,0)}$ (*a*) and $\mathscr{L}_{(2,0)}$ (*b*) for $Re = 3000$.

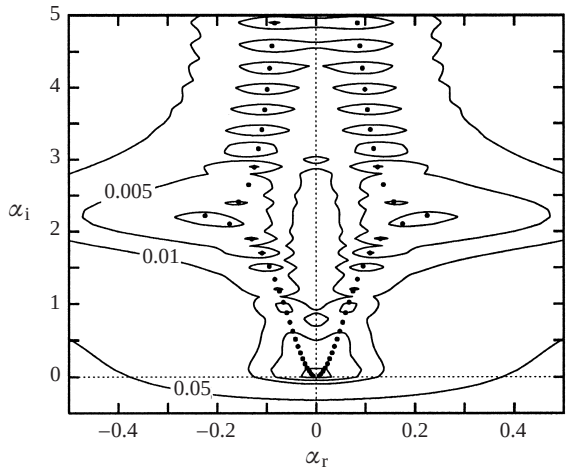

FIGURE 31. Spectrum and ϵ-pseudospectrum of $\mathscr{L}_{(2,0)}$ for $Re = 3000$. The small dots • represent the spectrum and the contour lines represent the outer boundaries of the ϵ-pseudospectrum.

regions does not indicate any transient growth. From this figure we can estimate $|\beta(10^{-1})| \sim 0.9$ which implies $\gamma_{10^{-1}} > 1$ so that the transient growth is possible. For more information about the ϵ-pseudospectrum and its relationship with transient growth for Hagen–Poiseuille flow, refer to Schmid & Henningson (1994).

Spectra for modes $(\pm 2, 0)$ *and* $(0, 0)$

In figure 30, the eigenspectra of $(m, n) = (0, 0)$ and $(2, 0)$ are shown for $Re = 3000$. The eigenspectrum of $(-2, 0)$ is as same as $(2, 0)$. The ϵ-pseudospectrum of $(2, 0)$ is shown in figure 31. We can estimate $|\beta(0.05)| \sim 0.3$ from the figure, so $\gamma_{0.05} > 1$ and transient energy growth is possible (see the previous subsection for the explanation of the ϵ-pseudospectrum).

B.3. *Evolution of the eigenmodes*

Spatial modes can propagate both downstream and upstream while growing or decaying. In principle we can judge the propagation properties of these modes by studying the group velocity $c_g = \partial\omega/\partial\alpha_r$ (see Drazin & Reid 1981, p. 345–353). The

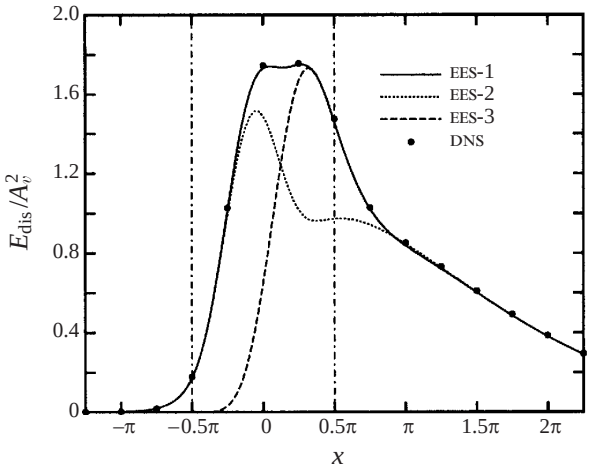

FIGURE 32. Spatial evolution of the disturbance energy $E_{\rm dis}(x;1,1)$ ($Re = 3000, \omega = 0.5$; two dash-dotted vertical lines indicate the disturbance region). For the DNS simulation, the disturbance amplitude $A_v = 10^{-3}$; for the eigenmode expansion solution of (3.7), there are three different realizations: EES-1: 1, 2-quadrant modes propagate downstream and 3, 4-quadrant modes upstream; EES-2: 1-quadrant modes propagate downstream and 3-quadrant modes upstream; EES-3: 1, 2-quadrant modes propagate downstream and no mode propagates upstream.

group velocity, however, can be computed only when the dispersion relation $\mathscr{F}(\omega, \alpha)$ is known which in our situation is not easy to find.

All experimental and theoretical results, however, suggest that Hagen–Poiseuille flow is linearly stable and this is supported by our own DNS results for $A_v \ll 1$. This implies that all eigenvalues in the 1- and 2-quadrants (i.e. $\alpha_{\rm i} > 0$) must be downstream propagating and all eigenvalues in the 3- and 4-quadrants (i.e. $\alpha_{\rm i} < 0$) upstream propagating. This has been checked by means of our EES. For the case EES-1 shown in figure 32, we have taken in (3.9) all eigenvalues in the 1- and 2-quadrants as downstream propagating and all eigenvalues in the 3- and 4-quadrants as upstream propagating. From the close agreement with the DNS results shown in figure 32, we conclude that our assumption regarding the propagation direction of the eigenvalues is indeed correct. Moreover, all eigenvalues are needed to obtain a good approximation of the flow. This is illustrated by case EES-2 also shown in figure 32 where only eigenvalues in the quadrants 1 and 3 have been taken into account. There is a clear difference for this case with the full DNS results especially in the neighbourhood of the perturbation region.

Although the upstream propagating modes have been seldom studied, they have been found also in other cases than Hagen–Poiseuille flow. For the boundary layer, upstream propagating modes have been studied by Ashpis & Reshotko (1990). These authors maintain that the upstream propagating modes decay much faster than the downstream propagating modes and this conclusion seems consistent with our results for Hagen–Poiseuille flow.

From figure 32 we see that when the upstream propagating modes are removed from the EES computation, i.e. case EES-3, there is no apparent difference in the disturbance energy of mode $(\pm 1, \pm 1)$ downstream of the perturbation region. This result should not lead us to the conclusion that the upstream propagating modes of $\mathscr{L}_{(\pm 1,\pm 1)}$ have no downstream effects at all since it is possible that by nonlinear interaction the upstream propagating modes may influence the downstream propagating modes. The occurrence

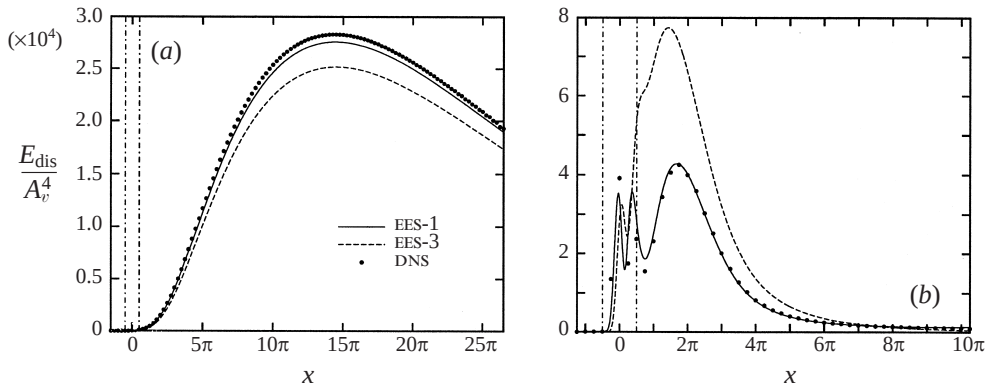

FIGURE 33. Spatial evolution of the disturbance energy for $Re = 3000, \omega = 0.5$. (*a*) $E_{\mathrm{dis}}(x; 2, 0)$; (*b*) $E_{\mathrm{dis}}(x; 0, 0)$. For the DNS simulation, the disturbance amplitude $A_v = 10^{-3}$; for the eigenmode expansion solution of (3.11), the interpretation of EES-1 and EES-3 are same as in figure 32.

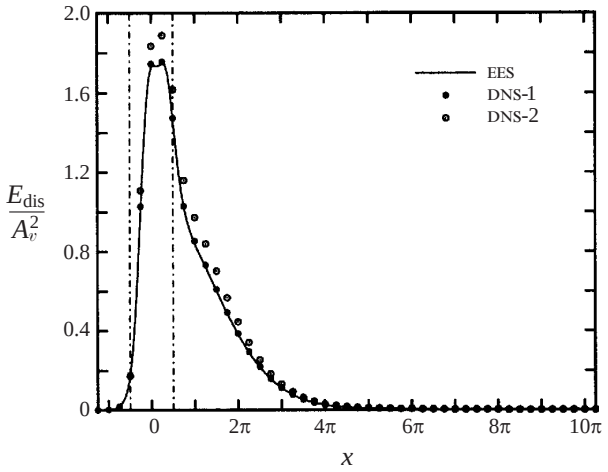

FIGURE 34. Spatial evolution of the disturbance energy $E_{\mathrm{dis}}(x; 1, 1)$ ($Re = 3000, \omega = 0.5$), where in DNS-1 the distance between the inflow and the left edge of PSB region is π, and in DNS-2 these two cross-sections coincide. The width of the PSB region $d = \pi$.

of this *downstream* effect of the *upstream* propagating modes is illustrated in figure 33 where the disturbance energy E_{dis} is given as a function of x for the modes $(0, 0)$ and $(\pm 2, 0)$ which are generated by the quadratic self-interaction of $(\pm 1, \pm 1)$. We see that the inclusion of the upstream propagating modes in the computation of $(\pm 1, \pm 1)$ has a clear influence on the magnitude of the $(0, 0)$ and $(\pm 2, 0)$ modes. Therefore, one should include all modes, both the upstream and downstream propagating ones, when one computes the evolution of the disturbance.

To realize that these upstream propagating modes exist is not only important for a better description of the disturbance evolution but it is also important for the implementation of our numerical simulations. Namely, in order to generate a non-reflecting outflow condition a fringe method has been used which is very efficient in damping the disturbances that propagate downstream out of the computational domain at the rightmost cross-section (see § 4.1, § 4.3). However, the fringe region

does not prohibit reflection of the upstream propagating modes at the leftmost cross-section (the inflow cross-section). Although the reflection is very weak, the generated noise can be amplified when it is propagating downstream. This has been investigated with help of a special DNS (DNS-2) for which the left edge of the PSB region coincides with the inflow cross-section, i.e. $x_c^* - \frac{1}{2}d = 0$ (see § 4.1 for a definition of x^*). The results are shown in figure 34. We see that the DNS-2 data differ from the EES results while the agreement with the EES is excellent for the DNS-1 data for which $x_c^* - \frac{1}{2}d = \pi$, i.e. the left edge of the disturbance region is still a distance π away from the left edge of the computational domain. In the latter case the upstream propagating modes can decay before the leftmost boundary is reached. Therefore, in all our numerical simulations we have used the location for the disturbance region as in DNS-1.

Appendix C. Derivation of (3.8) in §3

In this Appendix we provide the details of the eigenmode expansion procedure to obtain (3.8). Because the boundary condition (3.5) is non-homogenous for $(\pm 1, \pm 1)$, we have to pay special attention to the expansion of (3.4) because a direct substitution of (3.6) into (3.7) is not possible.

From the expansion (3.6) and the orthogonality relation (B 6) we obtain that

$$X_\alpha = \int_0^1 r \boldsymbol{G}_\alpha^\dagger \boldsymbol{F} \, \mathrm{d}r. \tag{C 1}$$

Suppose we can expand the left- and right-hand sides of (3.7) as

$$\frac{\partial \boldsymbol{F}}{\partial x} = \sum_\alpha Y_\alpha \boldsymbol{F}_\alpha, \quad \mathscr{L}\boldsymbol{F} = \sum_\alpha Z_\alpha \boldsymbol{F}_\alpha,$$

where the coefficient functions $Y_\alpha(x)$ and $Z_\alpha(x)$ will be determined in the following. As a result of the linear independence of different eigenmodes $\boldsymbol{F}_\alpha$, we then know that

$$Y_\alpha = Z_\alpha. \tag{C 2}$$

By applying the orthogonality relation (B 6) to $Y_\alpha(x)$ we find

$$Y_\alpha = \int_0^1 r \boldsymbol{G}_\alpha^\dagger \left(\frac{\partial \boldsymbol{F}}{\partial x} \right) \mathrm{d}r = \frac{\partial}{\partial x} \left(\int_0^1 r \boldsymbol{G}_\alpha^\dagger \boldsymbol{F} \, \mathrm{d}r \right) = \frac{\mathrm{d}X_\alpha}{\mathrm{d}x}.$$

Taking a similar approach and using the definition of $\mathscr{L}$ given by (B 1), we obtain

$$\begin{aligned} Z_\alpha &= \int_0^1 r \boldsymbol{G}_\alpha^\dagger (\mathscr{L}\boldsymbol{F}) \, \mathrm{d}r = \int_0^1 r \boldsymbol{G}_\alpha^\dagger \left(\mathscr{C}_0 \boldsymbol{F} + \mathscr{C}_1 \frac{\partial \boldsymbol{F}}{\partial r} + \mathscr{C}_2 \frac{\partial^2 \boldsymbol{F}}{\partial r^2} \right) \mathrm{d}r \\ &= \int_0^1 \left[(r \mathscr{C}_0^\dagger \boldsymbol{G}_\alpha)^\dagger \boldsymbol{F} + (r \mathscr{C}_1^\dagger \boldsymbol{G}_\alpha)^\dagger \frac{\partial \boldsymbol{F}}{\partial r} + (r \mathscr{C}_2^\dagger \boldsymbol{G}_\alpha)^\dagger \frac{\partial^2 \boldsymbol{F}}{\partial r^2} \right] \mathrm{d}r. \end{aligned}$$

By integrating by parts the first-order r-derivative term of the above equation, we find

$$\int_0^1 (r \mathscr{C}_1^\dagger \boldsymbol{G}_\alpha)^\dagger \frac{\partial \boldsymbol{F}}{\partial r} \, \mathrm{d}r = [(r \mathscr{C}_1^\dagger \boldsymbol{G}_\alpha)^\dagger \boldsymbol{F}]\big|_0^1 - \int_0^1 \frac{\mathrm{d}(r \mathscr{C}_1^\dagger \boldsymbol{G}_\alpha)^\dagger}{\mathrm{d}r} \boldsymbol{F} \, \mathrm{d}r,$$

and for the second-order r-derivative term

$$\int_0^1 (r\,\mathscr{C}_2^\dagger \mathbf{G}_\alpha)^\dagger \frac{\partial^2 \boldsymbol{F}}{\partial r^2}\,\mathrm{d}r = \left[-\frac{\mathrm{d}(r\,\mathscr{C}_2^\dagger \mathbf{G}_\alpha)^\dagger}{\mathrm{d}r}\boldsymbol{F} + (r\,\mathscr{C}_2^\dagger \mathbf{G}_\alpha)^\dagger \frac{\partial \boldsymbol{F}}{\partial r}\right]\Bigg|_0^1 + \int_0^1 \frac{\mathrm{d}^2(r\,\mathscr{C}_2^\dagger \mathbf{G}_\alpha)^\dagger}{\mathrm{d}r^2}\boldsymbol{F}\,\mathrm{d}r.$$

Combining these results we obtain

$$Z_\alpha = \int_0^1 \left[(r\,\mathscr{C}_0^\dagger \mathbf{G}_\alpha) - \frac{\mathrm{d}(r\,\mathscr{C}_1^\dagger \mathbf{G}_\alpha)}{\mathrm{d}r} + \frac{\mathrm{d}^2(r\,\mathscr{C}_2^\dagger \mathbf{G}_\alpha)}{\mathrm{d}r^2}\right]^\dagger \boldsymbol{F}\,\mathrm{d}r + \left[(r\,\mathscr{C}_1^\dagger \mathbf{G}_\alpha)^\dagger \boldsymbol{F} - \frac{\mathrm{d}(r\,\mathscr{C}_2^\dagger \mathbf{G}_\alpha)^\dagger}{\mathrm{d}r}\boldsymbol{F} + (r\,\mathscr{C}_2^\dagger \mathbf{G}_\alpha)^\dagger \frac{\partial \boldsymbol{F}}{\partial r}\right]\Bigg|_0^1.$$

Next we apply the definition for the adjoint operator given by (B 5) and (B 6) and the boundary conditions of $\mathbf{G}_\alpha$ and $\boldsymbol{F}$ given by (B 7) and (3.5). As a result we obtain

$$Z_\alpha = \int_0^1 r(\mathscr{L}^* \mathbf{G}_\alpha)^\dagger \boldsymbol{F}\,\mathrm{d}r + A_v C_\alpha f = \int_0^1 r\mathrm{i}\alpha \mathbf{G}_\alpha^\dagger \boldsymbol{F}\,\mathrm{d}r + A_v C_\alpha f = \mathrm{i}\alpha X_\alpha + A_v C_\alpha f,$$

where $C_\alpha = -\phi_{mn} G^*_{\alpha 1}|_{r=1}$ and where f is the PSB shape function (2.6). Finally from (C 2) we obtain

$$\frac{\mathrm{d}X_\alpha}{\mathrm{d}x} = \mathrm{i}\alpha X_\alpha + A_v C_\alpha f.$$

REFERENCES

Ashpis, D. E. & Reshotko, E. 1990 The vibrating ribbon problem revisited. *J. Fluid Mech.* **213**, 531–547.

Bergström, L. 1992 Initial algebraic growth of small angular dependent disturbances in pipe Poiseuille flow. *Stud. Appl. Maths* **87**, 61–79.

Bergström, L. 1993*a* Evolution of laminar disturbances in pipe Poiseuille flow. *Eur. J. Mech.* B/*Fluids* **12**, 749–768.

Bergström, L. 1993*b* Optimal growth of small disturbances in pipe Poiseuille flow. *Phys. Fluids* A **5**, 2170–2720.

Bergström, L. 1995*a* Nonlinear behaviour of transiently amplified disturbances in pipe Poiseuille flow. *Eur. J. Mech.* B/*Fluids* **14**, 719–735.

Bergström, L. 1995*b* Transient properties of a developing laminar disturbances in pipe Poiseuille flow. *Eur. J. Mech.* B/*Fluids* **14**, 601–615.

Bergström, L. 1998 Self-sustained amplification of disturbances in pipe Poiseuille flow. *Eur. J. Mech.* B/*Fluids* (submitted).

Boberg, L. & Brosa, U. 1988 Onset of turbulence in a pipe. *Z. Naturforsch.* **43a**, 697–726.

Canuto, C., Hussaini, M. Y., Quarteroni, A. & Zang, T. A. 1987 *Spectral Methods in Fluid Dynamics.* Springer.

Chung, Y. M., Sung, H. J. & Boiko, A. V. 1997 Spatial simulation of the instability of channel flow with local suction/blowing. *Phys. Fluids* **9**, 3258–3266.

Criminale, W. O., Jackson, T. L., Lasseigne, D. G. & Joslin, R. D. 1997 Perturbation dynamics in viscous channel flows. *J. Fluid Mech.* **339**, 55–75.

Danabasoglu, G., Biringen, S. & Streett, C. L. 1991 Spatial simulation of instability control by periodic suction blowing. *Phys. Fluids* A **3**, 2138–2147.

Darbyshire, A. G. & Mullin, T. 1995 Transition to turbulence in constant-mass-flux pipe flow. *J. Fluid Mech.* **289**, 83–114.

Dauchot, O. & Manneville, P. 1997 Local *versus* global concepts in hydrodynamic stability theory. *J. Phys.* II (*Paris*) **7**, 371–389.

Davey, A. 1978 On the stability of flow in an elliptic pipe which is nearly circular. *J. Fluid Mech.* **87**, 233–241.

Davey, A. & Nguyen, H. P. F. 1971 Finite-amplitude stability of pipe flow. *J. Fluid Mech.* **45**, 701–720.

Draad, A. A. & Nieuwstadt, F. 1998 The Earth's rotation and laminar pipe flow. *J. Fluid Mech.* **361**, 297–308.

Draad, A. A., Kuiken, G. & Nieuwstadt, F. 1998 Laminar-turbulent transition in pipe flow for Newtonian and non-Newtonian fluids. *J. Fluid Mech.* **377**, 267–312.

Drazin, P. G. & Reid, W. H. 1981 *Hydrodynamic Stability*. Cambridge University Press.

Eggels, J. G. M., Unger, F., Weiss, W. H., Westerweel, J., Adrian, R. J., Friedrich, R. & Nieuwstadt, F. T. M. 1994 Fully developed pipe flow: a comparison between direct numerical simulation and experiment. *J. Fluid Mech.* **268**, 175–209.

Eliahou, S., Tumin, A. & Wygnanski, I. 1998 Laminar-turbulent transition in Poiseuille pipe flow subjected to periodic perturbation emanating from the wall. *J. Fluid Mech.* **361**, 333–349.

Elofson, P. A. & Alfredson, P. H. 1998 An experimental study of oblique transition in plane Poiseuille flow. *J. Fluid Mech.* **358**, 177–202.

Garg, V. K. & Rouleau, W. T. 1972 Linear spatial stability of pipe Poiseuille flow. *J. Fluid Mech.* **54**, 113–127.

Gaster, M. 1965 On the generation of spatially growing waves in a boudary layer. *J. Fluid Mech.* **22**, 433–441.

Gill, A. E. 1965 On the behaviour of small disturbances to Poiseuille flow in a circular pipe. *J. Fluid Mech.* **21**, 145–172.

Goldstein, M. E. & Hultgren, L. S. 1989 Boundary-layer receptivity to long-wave free-stream disturbances. *Ann. Rev. Fluid Mech.* **21**, 137–166.

Henningson, D. S., Lundbladh, A. & Johansson, A. V 1993 A mechanism for bypass transition from localized disturbance in wall-bounded shear flows. *J. Fluid Mech.* **250**, 169–207.

Herbert, T. 1991 Exploring transition by computer. *Appl. Numer. Maths* **7**, 3–25.

Herron, I. 1991 Observations on the role of vorticity in the stability theory of wall bounded flows. *Stud. Appl. Maths* **85**, 269–286.

Joseph, D. D. & Carmi, S. 1969 Stability of Poiseuille flow in pipes, annuli and channels. *Q. Appl. Maths* **26**, 575–591.

Karniadakis, G. E., Israeli, M. & Orszag, S. A. 1991 High-order splitting methods for the incompressible Navier–Stokes equations. *J. Comput. Phys.* **97**, 414–443.

Kelvin, Lord 1887 Stability of fluid motion – Rectilinear motion of viscous fluid between two parallel planes. *Phil. Mag.* **24**, 188–196.

Kerswell, R. & Davey, A. 1996 On the linear instability of elliptic pipe flow. *J. Fluid Mech.* **316**, 307–324.

Kim, J., Moin, P. & Moser, R. 1987 Turbulence statistics in fully developed channel flow at low Reynolds number. *J. Fluid Mech.* **177**, 133–166.

Klebanoff, P. S., Tidstrom, K. D. & Sargent, L. M. 1962 The three-dimensional nature of boundary-layer instability. *J. Fluid Mech.* **12**, 1–34.

Kleiser, L. & Zang, T. A. 1991 Numerical simulation of transition in wall-bounded shear flows. *Ann. Rev. Fluid Mech.* **23**, 495–537.

Landahl, M. T. 1975 Wave breakdown and turbulence. *SIAM J. Appl. Maths* **28**, 735–756.

Lessen, M., Sadler, S. G. & Liu, T. Y. 1968 Stability of pipe Poiseuille flow. *Phys. Fluids* **11**, 1404–1409.

Lundbladh, A., Schmid, P. J., Berlin, S. & Henningson, D. S. 1994 Simulations of bypass transition for spatially evolving disturbances. In *AGARD-CP*-551, pp. 18.1–18.13.

Marcus, P. S. 1984 Simulation of Taylor–Couette flow. Part 1. Numerical methods and comparison with experiment. *J. Fluid Mech.* **146**, 45–64.

Nordström, J., Nordin, N. & Henningson, D. 1997 The fringe region technique and the Fourier-method used in the direct numerical simulation of spatially evolving viscous flows. *SIAM J. Sci. Comput.* (submitted).

Orszag, S. A. & Patera, A. T. 1983 Secondary instability of wall-bounded shear flows. *J. Fluid Mech.* **128**, 347–385.

O'Sullivan, P. L. & Breuer, K. S. 1994*a* Transient growth in circular pipe flow. I. Linear disturbances. *Phys. Fluids* **6**, 3643–3651.

O'Sullivan, P. L. & Breuer, K. S. 1994*b* Transient growth in circular pipe flow. II. Nonlinear development. *Phys. Fluids* **6**, 3652–3664.

Patera, A. T. & Orszag, S. A. 1981 Finite-amplitude stability of axisymmetric pipe flow. *J. Fluid Mech.* **112**, 467–474.

Reddy, S. C., Schmidt, P. J., Bagget, J. S. & Henningson, D. S. 1998 On the stability of streamwise streaks and transition thresholds in plane channel flows. *J. Fluid Mech.* **365**, 269–303.

Reynolds, O. 1883 An experimental investigation of the circumstances which determine whether the motion of water shall be direct or sinuous, and of the law of resistance in parallel channels. *Phil. Trans. R. Soc. Lond.* **174**, 935–982.

Rubin, Y., Wygnanski, I. & Haritonidis, J. H. 1980 Further observations on transition in a pipe. In *Laminar-Turbulent Transition. Proc. IUTAM Sym. Stuttgart* (ed. R. Eppler & H. Fasel), pp. 19–26. Springer.

Salwen, H., Cotton, F. W. & Grosch, C. E. 1980 Linear stability of Poiseuille flow in a circular pipe. *J. Fluid Mech.* **98**, 273–284.

Sandham, N. D. & Kleiser, L. 1992 The late stages of transition to turbulence in channel flow. *J. Fluid Mech.* **245**, 319–348.

Schmid, P. J. & Henningson, D. S. 1994 Optimal energy density growth in Hagen–Poiseuille flow. *J. Fluid Mech.* **277**, 197–225.

Schubauer, G. B. & Skramstad, H. K. 1947 Laminar boundary layer oscillations and transition on a flat plate. *J. Aero. Sci.* **14**, 69–76.

Shan, H., Ma, B., Zhang, Z. & Nieuwstadt, F. T. M. 1999 Direct numerical simulation of a puff and slug in transitional cylindrical pipe flow. *J. Fluid Mech.* **389**, 39–60.

Tatsumi, T. 1952 Stability of the laminar inlet-flow prior to the formation of Poiseuille regime, Part II. *J. Phys. Soc. Japan* **7**, 495–502.

Tomboulides, A. G., Israeli, M. & Karniadakis, G. E. 1989 Efficient removal of boundary-divergence errors in time-splitting methods. *J. Sci. Comput.* **4**, 291–308.

Trefethen, L. N., Trefethen, A. E., Reddy, S. C. & Driscoll, T. A. 1993 Hydrodynamic stability without eigenvalues. *Science* **261**, 578–584.

Tumin, A. 1996 Receptivity of pipe Poiseuille flow. *J. Fluid Mech.* **315**, 119–137.

Tumin, A. 1997 Laminar-turbulent transition in Poipeuille pipe flow subjected to periodic perturbation emanating from the wall. Part II: A theoretical consideration. Unpublished.

Waleffe, F 1995*a* Hydrodynamic stability and turbulence: beyond transients to a Self-sustaining process. *Stud. Appl. Maths* **95**, 319–343.

Waleffe, F. 1995*b* Transition in shear flows. Nonlinear normality *versus* non-normal linearity. *Phys. Fluids* **7**, 3060–3066.

Waleffe, F. 1997 On a self-sustaining process in shear flows. *Phys. Fluids* **9**, 883–890.

Wygnanski, I. J. & Champagne, F. H. 1973 On transition in a pipe. Part 1. The origin of puffs and slugs and the flow in a turbulent slug. *J. Fluid Mech.* **59**, 281–335.

Zang, T. A., Krist, S. E. & Hussaini, M. Y. 1989 Resolution requirements for numerical simulation of transition. *J. Sci. Comput.* **4**, 197–217.

Zikanov, O. Y. 1996 On the instability of pipe Poiseuille flow. *Phys. Fluids* **8**, 2923–2932.